UNIVERSITAT POLITÈCNICA DE CATALUNYA
BARCELONATECH
Escola d'Enginyeria de Telecomunicació
i Aeroespacial de Castelldefels

TREBALL DE FI DE GRAU

TFG TITLE: Guidance, Navigation and Control of a very small solar sail

DEGREE: Grau en Enginyeria d'Aeronavegació

AUTHOR: Carlos Díez García

ADVISOR: Jordi Gutiérrez Cabello

DATE: October 28, 2017

Títol: Guiatge, Navegació i Control d'una vela solar molt petita

Autor: Carlos Díez García

Director: Jordi Gutiérrez Cabello

Data: 28 d'octubre de 2017

Resum

Aquesta tesi de fi de grau es centra en l'estudi de l'estratègia de Guiatge, Navegació i Control (GNC) i el disseny del Subsistema de Determinació i Control d'Actitud (ADCS) d'una petita vela solar. La determinació i el control d'actitud d'una aeronau és essencial per al correcte desenvolupament d'una missió espaial. Aquesta tesi proposa l'ús de Dispositius de Reflectivitat Controlable (RCDs) pel control d'actitud en dos eixos i la implementació de l'algoritme recursiu d'estimació Optimal-REQUEST per la determinació d'actitud. El principal repte es troba en la feblesa del moment de força produït per la força de pressió per radiació solar. Els anàlisis numèrics que es realitzaran verificaran l'estabilitat de l'estratègia proposada.

Title : Guidance, Navigation and Control of a very small solar sail

Author: Carlos Díez García

Advisor: Jordi Gutiérrez Cabello

Date: October 28, 2017

Overview

This Final Degree Thesis, focuses on the study of the Guidance, Navigation and Control (GNC) strategy and the design of the Attitude Determination and Control Subsystem (ADCS) of a small solar sail. Spacecraft attitude and determination control is essential to successfully develop a space mission. This thesis propose the use of Reflective Control Devices for two-axis control and the application of the recursive estimate algorithm Optimal-REQUEST for attitude determination. The main challenge lies in the weakness of the torque produced by Solar Radiation Pressure force. Numerical analysis will be conducted to verify the stability of the proposed strategy.

¡Poyejali!

CONTENTS

LIST OF FIGURES

LIST OF TABLES

ACKNOWLEDGMENTS

I would like to express my gratitude to my thesis director, Dr. Jordi Gutiérrez Cabello who has been very helpful with his comments and recommendations about this thesis and has given me the opportunity to get to know the space sector.

Also I would like to thank my colleagues and friends Víctor Navarro Juárez and Carles Pié Rubió, with whom I have shared my stage in the university and have been a key piece in the realization of this project.

My thanks and love to my brother Raúl, who has been, is and will be my role model. And of course to my parents, Javier and María, who with a lot of patience have never doubt to give everything for me.

LIST OF ABBREVIATIONS

AU	Astronomical Unit
AD	Attitude Determination
ADCS	Attitude Determination and Control System
ADSS	Attitude Determination Subsystem
ACSS	Attitude Control Subsystem
CoM	Centre of Mass
CoP	Centre of Pressure
CVG	Coriolis Vibratory Gyroscope
DCM	Direct Cosine Matrix
EC	Electrochromic
GC	Geometrical Centre
IMU	Inertial Measurement Unit
LVLH	Loval-Vertical / Local-Horizontal
MEMS	Micro-machined Electro-Mechanical Systems
MOI	Moment Of Inertia
PD	Proportional Derivative
RCD	Reflective Control Device
SRP	Solar Radiation Pressure
VEECD	Variable Emittance Electro-Chromic Device
VED	Variable Emittance Device

GENERAL INTRODUCTION

Propulsion devices are one of the most restrictive subsystems in small satellites, many of them even showing a complete lack of them. In this set of three Final Degree Thesis, we have explored the possibility of using a small solar sail to propel a femtosatellite.

As solar sails employ solar radiation pressure, do not carry any kind of hazardous materials (as would happen in most of the rest of propulsion systems), and therefore would have no constraints to be launched as a secondary payload.

Solar sails have been known to be feasible for a long time, but practical implementation was precluded until recently due to its difficult construction and deployment. As they use the pressure exerted by solar light, solar sails do not require to carry any kind of fuel and, as long as they remain illuminated by the Sun, they can propel themselves for an indefinitely long time.

The first solar sails were IKAROS, launched by JAXA in 2010, and Nanosail-D, launched by NASA in 2011. In both cases, the missions were a complete success. IKAROS is especially relevant in this regard because its mission took it to the orbit of Venus, thus probing not only that the propulsion mechanism was physically sound, but also technologically feasible. Several solar sails projects are currently underway; the most salient is Lightsail-2, developed by The Planetary Society.

Its main strength is also its most important weakness: by using the tiny force exerted by light pressure, their fabric must be extremely light, and thus require a very flimsy material. Even in our case, with a very small sail of just 10 m^2, it is impossible to launch the sail deployed. Hence, a mechanism to fold it on the ground, and allow an easy (and unsupervised) unfolding once in space, must be devised. The fabric composing the sail must also be protected against rips and deep wrinkles, something quite difficult with such a delicate material.

The payload for our sail, that we have christened FemtoSail, will accordingly be very low-mass. The bus of the active part of the FemtoSail will have a mass under 50 grams. Our goal is to have as high an acceleration as possible and obviously this calls for a very small total mass. The total mass of the sail will be, at most, 100 grams.

FemtoSail will be folded and carried into orbit inside a canister with the same form factor as a 3U CubeSats (then, a rectangular prism with a base 10 cm in side, and a long side of 30 cm). Once in orbit, the canister will open a hatch and the sail will be ejected. After the ejection, the solar sail must unfold by itself.

The general layout is as follows: the sail will be square in shape, and the bus will be composed of an on board computer, a battery that will store the energy gathered by solar cells, a flat antenna and transmitter, and electrochromic systems to allow attitude control. As the energy gathered by the solar cells would be quite reduced, communications would be of the burst kind.

The mission for such a small spacecraft must be compatible with its capabilities, that due to its very low mass are rather limited. It is equally important to consider in which regards a set of femtosatellites would provide an advantage as compared to standard satellites. A sensible option is to have a large number of femtosatellites to carry out a determination of some property in multiple points. As an example, we will focus on their use as probes of

the Earth's magnetotail. Magnetospheric physics has been one of the main focus of Space Science since the very beginning of Human exploration of the environments of the Earth. However, the number of satellites involved in this kind of investigations has always been quite small, and usually restricted to Low Earth Orbit. Our mission would determine the magnetic field strength and some plasma properties simultaneously in several points.

Using a solar sail with manoeuvring capabilities would constitute a valuable asset, as it would be possible to make several scans or particular zones of the magnetosphere without waiting for the orbital motion allow for a new pass through the region of interest.

The magnetosphere is a very dynamic region, with multiple physical phenomena deploying simultaneously, and its study is very involved. Having good quality data in many different (albeit nearby) points would allow a deeper understanding of the processes going on.

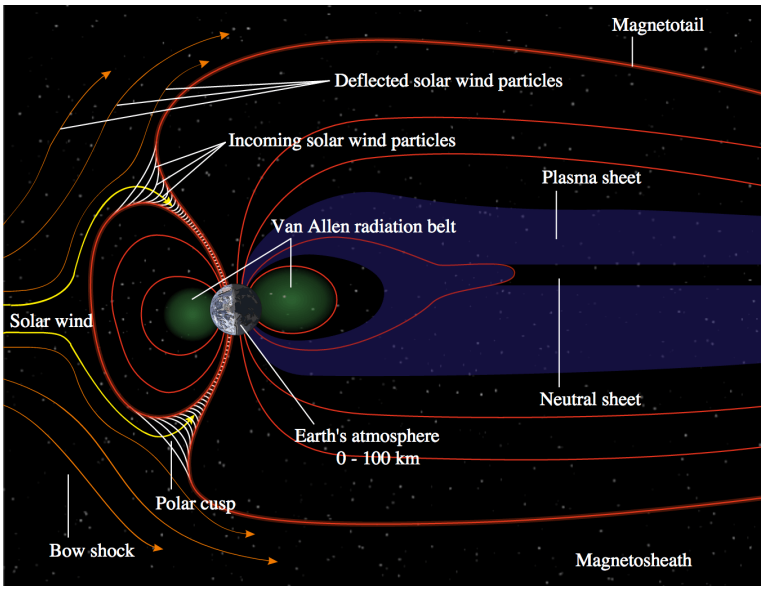

Figure 1: Schematics of the magnetosphere of the Earth and its interaction with the solar wind. The magnetotail is the region in purple to the right of the Earth.

The magnetotail is an ill-known part of the magnetosphere, observed basically in the Lunar environment, both from orbit as well as from the surface. However, the dynamics and properties of the magnetic field of the Earth beyond the Moon orbit is uncharted waters.

The solar wind stretches out the terrestrial magnetic field into an elongated and dynamic structure. Just a few missions have observed this region, the most remarkable ones are ISEE-3 (International Sun-Earth Explorer 3), and Geotail. Both were able to observe the magnetotail up to a distance of 200–220 Earth radii, finding that the plasma sheet is still well-defined at these distances.

The magnetotail is composed of two lobes, one above the other below the equatorial plane, where the magnetic field lines are almost parallel. Here the plasma density is low, and at large distances from the Earth, they are penetrated by the solar wind. Eventually, the weakening magnetic field of the Earth becomes attached to the interplanetary magnetic field, allowing the plasma in the lobes to escape.

Between the lobes there is a region on weak magnetic field and relatively high plasma density, the plasma sheet. Its width ranges from 2 to 6 Earth radii, and it also extends

to very long distances (around 200 Earth radii). As the magnetic field here is weak, the plasma moves more freely than in the case of the lobes. There is a cross tail current flowing across the plasma sheet in the dawn-dusk sense; this electrical current is responsible of generating the local magnetic field. Two currents, flowing through the magnetopause on the north and south lobes, close the circuit. The central part of this region is almost neutral, and is called the neutral sheet.

As the plasma sheet is continuously loosing plasma to the interplanetary medium, it is necessary some replenishment mechanism. While there are several hypotheses, the actual mechanism remains difficult to explain. A set of simultaneous measurements in multiple locations could greatly help to ascertain its nature.

The goal of this work is to provide a very basic, low-cost system to provide in-situ measurements of the magnetic field in this region. One very basic difficulty for a classical satellite would be the scarcity of missions allowing a secondary payload launch. In the case of solar sails, the initial orbit is not that important, as their propulsive capabilities allow them to navigate to achieve the final orbit (even if the time required to do so can be substantial).

As will be described further on, the envisioned mission carries a MEMs magnetometer to determine the magnetic field in different location of the magnetotail, near its neutral sheet.

This thesis work is a part of a series of three Final Degree Thesis simultaneously carried on to generate a full pre-A phase description. Then, the introduction up to this point is shared with the other two Degree Thesis (titled *Design and test of the bus of a very small solar sail* and *Design, deployment mechanism, and thermal control of a very small solar sail*).

INTRODUCTION

This Final Degree Thesis, focuses on the study of the Guidance, Navigation and Control (GNC) strategy and the design of the Attitude Determination and Control Subsystem (ADCS) of a small solar sail. The technological advance and the miniaturization of the electronics (MEMS technology) has led to the investigation of new space propulsion methods.

The concept of solar sailing dates back to the Soviet pioneers of astronautics, although in terms of femtosatelites transportation has been tested successfully in the last decade. it is based, as the rest of conventional propulsion systems, in Newton's third law, although the momentum gain comes from an environmental source, the Sun. Since solar sails do not use any finite reaction mass, they can provide continuous acceleration limited only by the lifetime of the sail film in the space environment. These propulsion capabilities allow them to reach any desired orbit, although the time required for it may be substantially high.

Throughout the thesis we will see that the force exerted by the photons that impact on the sail film is very weak, reason why the most limiting requirement of the mission is the total mass of the FemtoSail. On the other hand, the greater the area of the sail exposed to visible solar radiation, the greater number of photons are intercepted. Therefore, the parameters chosen for the design of a solar sail depend directly on the needs and constraints of the mission.

The correct development of the scientific part of the mission, which consist of the measurement of magnetic field in the magnetotail, is influenced by the knowledge and precise control of the position and orientation of the Femtosail in space. The Attitude Determination and Control Subsystem is the responsible of this task. The position and attitude determination will be performed from the data acquisition of gyroscopes, accelerometers and sun sensor and the use of recursive attitude estimation algorithms. A precise attitude determination is essential so that the control subsystem can meet mission pointing requirements. In particular, the FemtoSail is required to point towards the Sun to guarantee the power supply to the rest of the subsystems.

The SRP force depends directly on the optical properties of the material on which the force is exerted. Therefore, the development of new MEMS technologies and materials capable of varying their optical properties according to an applied electric potential, allow the investigation of new attitude control methods. These actuators, which are known as Reflective Control Devices (RCDs), meet the strict requirements of mass and power, and for that reason are proposed for the attitude control of the FemtoSail. The algorithm that governs the control subsystem will be a linear proportional derivative control law defined to achieve the desired attitude while the angular rate is reduced to zero.

Due to the need to introduce the reader into the solar sailing context, chapter 1 provides the fundamentals of solar radiation propulsion and design parameters. Chapter 2 presents the attitude kinematics and dynamics in its quaternion representation. Chapters 3 and 4 will be focussed on the description and design of the determination and control subsystems respectively. Following, Chapter 5 is devoted to the theoretical and numerical analysis of the ADCS presented before. Finally, thesis conclusions can be found in chapter 6.

CHAPTER 1. FUNDAMENTALS OF SOLAR SAILING

1.1. Solar Radiation Pressure

Solar Radiation Pressure (SRP) is the source of motive force given by the momentum transported to the sail by radiative energy from the sun. This radiative energy, which we perceive as light, can push matter as it happens with dust tails of comets or interplanetary dust swept out by SRP. In this section it will be presented two physical descriptions of the momentum transfer process

1.1.1. Quantum description

In quantum mechanics is considered that light is composed by packets of energy known as photons which are capable to transport momentum. Investigations of Max Plank during the beginning of twentieth century about the theoretical explanation of the energy radiated by a black body as a function of the wavelength results in the concept of photon. Plank considered that radiative energy must be quantised at discrete levels although is propagated as a wave after emission. Instead, Einstein proposed that radiative energy was emitted and absorbed in discrete packets giving an explanation for the observations of photoelectric effect.

Mathematically, the energy transported by a photon can be described by Planck's law

$$E = h \cdot \nu \tag{1.1}$$

where E is the energy transported, h is Planck constant and ν the frequency of photon.

The mass-energy equivalence of special relativity allows to write E as

$$E^2 = m_0^2 c^4 + p^2 c^2 \tag{1.2}$$

where m_0 is the rest mass of the particle, c is the speed of light and p is the momentum of particle. Since a photon has zero rest mass, its energy may be written as

$$E = p \cdot c \tag{1.3}$$

The momentum transported by a photon is given by 1.1 and 1.3

$$p = \frac{h \cdot \nu}{c} \tag{1.4}$$

The pressure exerted over the solar sail is produced by the momentum transported by a photon flux emitted from the sun. Therefore it has to be defined an energy flux W at a distance r from the sun. Since distance between sun and solar sail is much bigger than solar radius, the Sun can be considered as a point radiation source producing parallel solar rays.

$$W = W_E \left(\frac{R_E}{r} \right)^2 \tag{1.5}$$

$$W_E = \frac{L_s}{4\pi R_E^2}$$

where W_E is the energy flux measured at the Earth, R_E is the distance between Sun and Earth (1 AU), r is the distance between Sun and solar sail and L_s is the solar luminosity.

From 1.5 the energy transported δE across a surface of area A in time δt is

$$\Delta E = W \cdot A \cdot \Delta t \tag{1.6}$$

From 1.3 the momentum transported δp is

$$\Delta p = \frac{\Delta E}{c} \tag{1.7}$$

Therefore considering the pressure P exerted over the solar sail as the momentum transported per unit time, per unit area, we have

$$P = \frac{1}{A}\left(\frac{\Delta p}{\Delta t}\right) = \frac{W}{c} \tag{1.8}$$

SRP depends on optical properties of the solar sail surface and orientation. The most simplified case is the one in which all photons are reflected towards the sun parallel to the surface normal vector of the solar sail. Thus, incident and reflected photons transfer moment.

$$P_{max} = 2 \cdot P = \frac{2W}{c} \tag{1.9}$$

1.1.2. Electromagnetic description

In electromagnetism light can be described as electromagnetic radiation which propagates through space as waves. Electromagnetic radiation is capable to transport momentum as stated by Maxwell in his *Treatise on Electricity and Magnetism*.

> Hence in a medium in which waves are propagated there is a pressure in the direction normal to the waves and numerically equal to the energy in unit volume. *Maxwell 1873*

The electric field component E of the wave generates a current j on the incident surface. Together with the magnetic field component Lorentz force is generated on the direction of electromagnetic wave propagation.

$$\delta f = j_z B_y \, \delta x \delta y \delta z \tag{1.10}$$

The pressure exerted will be the Lorentz force per unit area

$$\delta P = j_z B_y \, \delta x \tag{1.11}$$

From Maxwell's equations the mean value of pressure as function of time is

$$\langle \delta P \rangle = -\frac{\Delta}{\Delta x} U \delta x \tag{1.12}$$

where U is defined as the energy density for the electric and magnetic components

$$U = \frac{1}{2}\varepsilon_0 E^2 + \frac{1}{2\mu_0} B^2 \tag{1.13}$$

where ε_0 and μ_0 are permittivity and permeability of free space respectively. Energy density can be written as energy per unit volume. Considering two plane waves separated by distance Δx incident on a surface of area A, the volume between waves is $A \cdot \Delta x$. Therefore,

$$U = \frac{\Delta E}{A\Delta x} = \frac{\Delta E}{a \cdot (c\Delta t)} \tag{1.14}$$

The flux of energy is given by

$$W = \frac{1}{A} \cdot \left(\frac{\Delta E}{\Delta t} \right) \tag{1.15}$$

From 1.14 and 1.15 it can be seen that

$$U = \frac{W}{c} \tag{1.16}$$

Integrating 1.12 for a surface of thickness Δl it can be obtained the pressure exerted on the solar sail.

$$\langle P \rangle = -\int_0^{\Delta t} \frac{\delta U}{\delta x} \delta x = \langle U \rangle = \frac{W}{c} \tag{1.17}$$

As can be seen 1.8 and 1.17 are the same expression an thus it can be concluded that quantum and electromagnetic description of SRP are equivalent.

1.2. Optical model

In a more realistic solar sail model it is necessary to define a mathematical model that takes into account the interaction between photons and solar sail such as the geometry, the temperature, the illuminated area or the optical properties of the sail material.

As described above, SRP is generated by those photons that impact the surface of the solar sail. Thus, the optical properties of the material determine the effects of transmission, absorption and reflection. The probability that one of these effects occurs must be such that

$$\tau + \alpha + \rho = 1 \tag{1.18}$$

where τ, a and ρ denote the probability for transmission, absorption and reflection respectively.

1.2.1. Transmission force

Transmitted photons do not transfer moment to solar sail and thus the generated force is equal to zero.

$$F_\tau = 0 \tag{1.19}$$

1.2.2. Absorption force

Absorbed photons generate a force on incidence direction (unit vector $\vec{u}$) due to momentum transfer.

$$f_a = \frac{\delta P}{\delta t}\vec{u} = \frac{1}{c}\frac{\delta E}{\delta t}\vec{u} = \frac{W}{C}\cos\theta\,\delta S\,\vec{u} = PAcos\theta\,\vec{u} \tag{1.20}$$

Some of those absorbed photons are re-radiated on $\vec{n}$ direction through solar sail surface as infrared radiation due to surface temperature. Assuming thermal balance and uniform temperature,

$$W\cos\theta = (\varepsilon_f + \varepsilon_b)\sigma T_{eq}^4 \tag{1.21}$$

From 1.21 it can be obtained the sail equilibrium temperature as

$$T_{eq} = \sqrt[4]{\frac{\alpha W\cos\theta}{\sigma(\varepsilon_f + \varepsilon_b)}} \tag{1.22}$$

Thus, the resultant force due to emitted photons is given by

$$f_e = \frac{\sigma T^4}{c}(\varepsilon_f B_f + \varepsilon_b B_b)\,\delta S\,\vec{n} = \alpha\frac{W\cos\theta}{c}\frac{\varepsilon_f B_f - \varepsilon_b B_b}{\varepsilon_f + \varepsilon_b}\,\delta S\,\vec{n} = \tag{1.23}$$

$$= PA\,\alpha\cos\theta\frac{\varepsilon_f B_f - \varepsilon_b B_b}{\varepsilon_f + \varepsilon_b}\,\vec{n}$$

where B is Lambert coefficient of surface, ε are the emissivities and f and b are the subscripts used to denote the front and back surfaces respectively. In a simplified case where the front and back surfaces were equal, the resultant force would be zero.

From 1.20 and 1.23 it can be write the total force generated by absorbed and emitted photons as

$$\alpha F_a = f_a + f_e = PA\cos\theta(\vec{u} + \alpha\frac{\varepsilon_f B_f - \varepsilon_b B_b}{\varepsilon_f + \varepsilon_b}\vec{n}) \tag{1.24}$$

1.2.3. Reflection force

On the other hand, a fraction of incident photons are reflected exerting a force on reflection direction. Reflected radiation can be assumed specular (subscript *s*) or diffuse (subscript *d*).

From 1.26 and 1.34 it can be defined the total force generated by reflected photons as

$$\rho F_\rho = \rho_s f_s + \rho_d f_d = \rho_s(-PA\cos\theta\,\vec{s}) + \rho_d(PA\cos\theta\,B_f\,\vec{n}) \tag{1.25}$$

1.2.3.1. Specular reflection

Specular reflection depends on surface irregularities and it is the responsible of the shine of an object. The force exerted has $-\vec{s}$ direction.

$$f_s = \frac{W}{c}\cos\theta\,\delta S(-\vec{s}) = -PA\cos\theta\,\vec{s} \tag{1.26}$$

1.2.3.2. Diffuse reflection

Diffuse reflection is generated by scattered photons in all directions. The force exerted has $\vec{n}$ direction. Mathematically this phenomenon can be modelled using Lambert diffusion which states that radiant intensity of reflected photons when viewed from an angle γ is proportional to $\cos\gamma$.

Being a differential area $\delta\Omega$,

$$\delta\Omega = \delta\gamma\delta\varphi \sin\gamma R^2 \tag{1.27}$$

Radiant intensity on $\delta\Omega$ will be

$$I_\Omega = I_{max}\cos\gamma \tag{1.28}$$

where I_{max} is the maximum radiant intensity obtained from the conservation of radiant flux. The total radiant flux is the sum of all radiant intensity over the entire hemisphere:

$$W\cos\theta\,\delta S = \int I_\Omega \delta\Omega = \int I_{max}\cos\gamma\,\delta\Omega = \int_0^{\frac{\pi}{2}}\int_0^{2\pi} I_{max}\cos\gamma\sin\gamma R^2\,\delta\varphi\delta\gamma = \tag{1.29}$$

$$= 2\pi R^2 I_{max}\int_0^{\frac{\pi}{2}}\cos\gamma = \pi R^2 I_{max}$$

Therefore maximum radiant intensity can be written as

$$I_{max} = \frac{W\cos\theta\,\delta S}{\pi R^2} \tag{1.30}$$

The radiative flux on differential area is

$$W_{\delta\Omega} = I_\Omega\delta\Omega = \frac{W\cos\theta\delta S}{\pi R^2}\cos\gamma\sin\gamma R^2\,\delta\gamma\delta\varphi \tag{1.31}$$

Thus, the resultant force on differential area is

$$f_{\delta\Omega} = \frac{W_{\delta\Omega}}{c} = \frac{W\cos\theta\,\delta S}{\pi c}\cos\gamma\sin\gamma\delta\gamma\delta\varphi \tag{1.32}$$

Integrating over cone volume it can be written the total resultant force as

$$f_d = \int_0^{\frac{\pi}{2}}\int_0^{2\pi}\cos\gamma d_{\delta\Omega}\,\vec{n} = \int_0^{\frac{\pi}{2}}\int_0^{2\pi}\frac{W\cos\theta\delta S}{\pi c}\cos^2\gamma\sin\gamma\delta\gamma\delta\varphi\,\vec{n} = \frac{2}{3}\frac{W\cos\theta\delta S}{c}\,\vec{n} \tag{1.33}$$

where $\frac{2}{3}$ factor characterize a Lambertian surface and can be substituted by B_f for non-Lambertian surfaces. Consequently, the resultant force can be rewritten as

$$f_d = \frac{W}{c}\cos\theta\,\delta S\,B_f\,\vec{n} = PA\cos\theta\,B_f\,\vec{n} \tag{1.34}$$

1.2.4. Total force

The total force exerted over the solar sail is given by

$$F_{total} = \tau F_\tau + \alpha F_a + \rho F_\rho \tag{1.35}$$

where F_τ is the force due to transmission, F_a is the force due to absorption and emission and F_ρ is the force due to reflection. Substituting 1.19, 1.24 and 1.25 into above expression

$$F_{total} = (PA\cos\theta\,\vec{u} + PA\,\alpha\,\cos\theta\,\frac{(\varepsilon_f B_f - \varepsilon_b B_b)}{(\varepsilon_f + \varepsilon_b)}\,\vec{n}) \tag{1.36}$$

$$+\rho_s(-PA\cos\theta\,\vec{s}) + \rho_d(PA\cos\theta\,B_f\,\vec{n})$$

By doing some algebra the total force can be write as

$$F_{total} = PA \cdot (\cos\theta\,\vec{u} + \alpha\cos\theta\,\frac{(\varepsilon_f B_f - \varepsilon_b B_b)}{(\varepsilon_f + \varepsilon_b)}\,\vec{n} \tag{1.37}$$

$$-\rho_s\cos\theta\,\vec{s} + \rho_d\cos\theta\,B_f\,\vec{n})$$

SRP has a component on the normal direction (denoted by $\vec{n}$) an a component on the tangential direction (denoted by $\vec{t}$). Then it can be defined $\vec{s}$) and $\vec{u}$) directions as a function of normal and tangential components.

$$\vec{u} = \cos\theta\,\vec{n} + \sin\theta\,\vec{t} \tag{1.38}$$

$$\vec{s} = -\cos\theta\,\vec{n} + \sin\theta\,\vec{t} \tag{1.39}$$

Replacing 1.38 and 1.39 into 1.37 it is obtained the following expression

$$F_{total} = PA \cdot (\cos\theta\,(\cos\theta\,\vec{n} + \sin\theta\,\vec{t}) + \alpha\cos\theta\,\frac{(\varepsilon_f B_f - \varepsilon_b B_b)}{(\varepsilon_f + \varepsilon_b)}\,\vec{n} \tag{1.40}$$

$$-\rho_s\cos\theta\,(-\cos\theta\,\vec{n} + \sin\theta\,\vec{t}) + \rho_d\cos\theta\,B_f\,\vec{n})$$

Therefore the normal and tangential component are defined respectively as

$$F_{normal} = PA \cdot (\cos^2\theta + \alpha\cos\theta\frac{(\varepsilon_f B_f - \varepsilon_b B_b)}{(\varepsilon_f + \varepsilon_b)} + \rho_s(\cos^2\theta) + \rho_d B_f\cos\theta)\,\vec{n} \tag{1.41}$$

$$F_{tangential} = PA \cdot (\cos\theta\sin\theta\,(1-\rho_s))\,\vec{t} \tag{1.42}$$

Total force vector due to SRP can be defined as

$$F_{total} = \sqrt{F_n^2 + F_t^2}\,\vec{m} \tag{1.43}$$

where $\vec{m}$ is the unit vector in the total force direction. Since the force generated by absorbed photons is greater than by those reflected, total force direction won't be coincident with $\vec{n}$. The angle between $\vec{m}$ and $\vec{n}$ is

$$\phi = \arctan\frac{F_t}{F_n} \tag{1.44}$$

1.3. Performance metrics

In order to evaluate solar sail designs specific performance metrics are defined. Characteristic acceleration is the fundamental metric and determines the transfer time to a particular target or whether an orbit is possible. Characteristic acceleration is defined as the SRP acceleration experienced by solar sail oriented normal to the Sun-line at a distance of 1AU.

$$a_0 = \frac{2P_{1AU}\,\eta}{\sigma} \tag{1.45}$$

where $2P$ denotes the maximum SRP exerted on solar sail since it is oriented normal to the Sun-line, η is the efficiency for a non-perfect optical properties (billowing, transparency, lambertianity...) and σ is the sail loading which may be written as

$$\sigma = \frac{m}{A} \tag{1.46}$$

being *m* and *A* the total solar sail mass and area respectively.

The lightness factor is the ratio of characteristic acceleration and Sun's local gravity at 1AU and it is useful to define the possible orbits:

$$\lambda = \frac{a_0}{g_{1AU}} \tag{1.47}$$

Sun's local gravity can be computed with Newton's law of universal gravitation,

$$g = G\frac{M}{r^2} \tag{1.48}$$

where $G = 6.67408 \times 10^{-11}$ $m^3 \cdot kg^{-1} \cdot s^{-2}$ is the gravitational constant, $M = 1.98855 \times 10^{30}$ kg is the mass of the Sun and $r = 149.5978707 \times 10^9$ m is 1AU.

Mission	Sail mass [kg]	Sail area [m^2]	σ_0 [g m^{-2}]	a_0 [mm s^{-2}]	$\lambda\ (\times 10^{-2})$
FemtoSail	540.77 $\times 10^{-3}$	10	54.08	0.14	2.41
IKAROS	315	196	1607.14	4.82 $\times 10^{-3}$	0.08
HELIOS	18.3	990	18.49	0.42	7.07
NanoSail-D	4	10	400	0.02	0.33
LightSail	4.5	32	140.63	0.06	0.93
Sunjammer	32	1200	26.67	0.29	4.90
ASPEN	21	1225	17.14	0.45	7.63

Table 1.1: Comparison of solar sail performance metrics for $\eta = 0.85$

Since solar sails do not eject any reaction mass as propulsion method, the theoretical specific impulse is infinite. To compare with other propulsion systems the Tsiolkovsky rocket equation has to be modified. The effective Δv can be represented as function of characteristic acceleration and mission duration. The final-initial mass ratio can be written as payload mass fraction of the solar sail:

$$I_{sp} = \frac{\Delta v}{g_{SL}}\, ln\left(\frac{m_s + m_p}{m_p}\right)^{-1} \sim \frac{a_0 t_m}{g_{SL}}\, ln\left(\frac{m_s + m_p}{m_p}\right)^{-1} \tag{1.49}$$

It should be noted that characteristic acceleration will vary during the mission due to the sail orientation. Moreover, specific impulse increases linearly with mission duration, so solar propulsion systems are competitive for long-duration missions.

Engine	Type	Propellant	Specific Impulse [s]
FemtoSail	Solar	-	$43.66_{/year}$
AESTUS	Hypergolic liquid rocket	N_2O_4/MMH	324
RL-10B-2	Cryogenic liquid rocket	LH_2/LOX	462
HiPEP	Ion thruster	Xenon	9620 @39.3kW
PPS-1350	Hall thruster	Xenon	1650 @1.5kW
VASIMR	Electro-magnetic thruster	Argon	5000 @200kW

Table 1.2: Comparison of propulsion systems

1.4. Solar sail specific attitude control methods

Methods specifically developed for attitude control on solar sails are based on distance between mass and pressure centres. Centre of Mass (CoM) is the geometric point which moves as a particle of mass equal to total mass of the system subject to resultant forces acting on the system. Centre of Pressure (CoP) is the geometric point where the resultant force produced by pressure field is applied.

As function of CoM and CoP position on the longitudinal axis, the system can be statically stable (CoM between CoP and Sun) or unstable (CoM behind CoP). Furthermore, separating both centres on X-Y plane of the solar sail it is obtained a distance between application point of force and centre of mass, i.e. a torque.

1.4.1. Control vane method

Control vane method is based on CoP displacement w.r.t. fixed CoM. Sailcraft has vanes attached to the end tip of the diagonal booms to have a large momentum arm and thus provide large torque. These vanes are made out of the same reflective material as the sail and have two rotational degrees of freedom. Rotation of vanes results in movement of CoP and thus in generation of control torque.

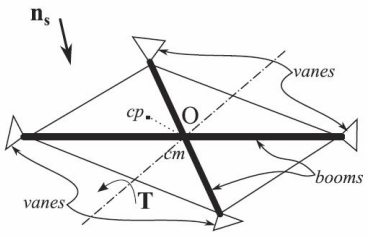

Figure 1.1: Control vane method schematic

1.4.2. Tilted wings method

Tilted wings method is based on sail plane tilting. Solar sail surface is attached to rotatable booms, each having one rotational degree of freedom. By rotating the booms sail plane is tilted and torque is generated to control Roll, Pitch and Yaw.

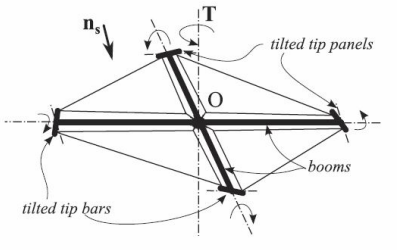

Figure 1.2: Tilted wings method schematic

1.4.3. Gimbaled masses method

Gimbaled masses method is based on CoM displacement. In this case, a mass is attached to a solar sail through a rigid rod having two rotational degrees of freedom (θ and ϕ). Assuming that CoM lies on the sail plane, when the mass position changes CoM shifts to a new position generating a torque to control Roll and Pitch. The effectiveness of this

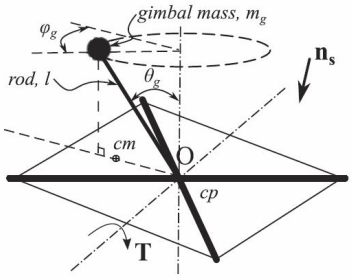

Figure 1.3: Gimbaled masses method schematic

method is higher under presence of gravity gradient disturbance force. In addition it is recommended to use the payload mass as the gimbaled mass.

1.4.4. Reflectivity control method

Reflectivity control method is based on CoP offset w.r.t. fixed CoM. There are devices that can vary their optical properties depending on the voltage applied. Therefore, SRP force can be modulated to shift CoP out of the normal position which normally coincides with CoM. Placing those devices at the outer edge of the sail surface, generated torque is maximized.
By using reflectivity control devices (RCDs), attitude control is performed without moving

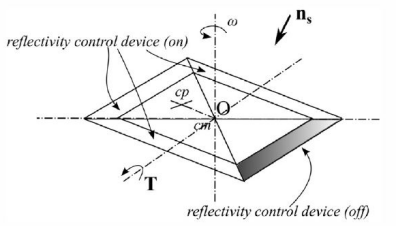

Figure 1.4: Reflectivity control method schematic

parts which improves the reliability of the system. Moreover, due to the low weight and low consumption the restrictive requirements of mass and power are fulfilled.

As a first approximation and for simplification it will be considered that CoM is fixed and coincident with geometrical centre (GC). Thus, the method applied will use thrust vector control to shift the CoP with regards to a fixed CoM to produce the required control torques. In section 4.1. the use of RCDs for attitude control is proposed and discussed.

CHAPTER 2. ATTITUDE KINEMATICS AND DYNAMICS

2.1. Reference frames

Reference frames are defined by a set of three orthogonal unitary vectors and are characterized by its origin or position from which the system is observed and the orientation of axes. Reference frames can be classified as Inertial or Non-Inertial.

Inertial frames move at constant velocity without rotation with respect to stars. On the other hand, Non-Inertial frames are undergoing acceleration (which could include rotation) with respect to an inertial frame.

2.1.1. Local Vertical Local Horizontal frame

Local-Vertical/Local-Horizontal (LVLH) frame is a Non-Inertial frame which is referenced to the spacecraft's orbit. It has its *+z* axis pointing along sun vector, its *+y* axis pointing along the negative orbit normal and its *+x* axis completes the right-handed triad.

2.1.2. Spacecraft Body frame

Spacecraft body frame is the Non-Inertial frame defined such that its origin is coincident with the geometrical centre of solar sail, its *+z* axis is aligned with the negative solar sail normal, its *+x* axis is aligned with the solar sail tangential and its *+y* forms a right-handed triad.

In the nominal configuration, body axes are aligned with LVLH axes.

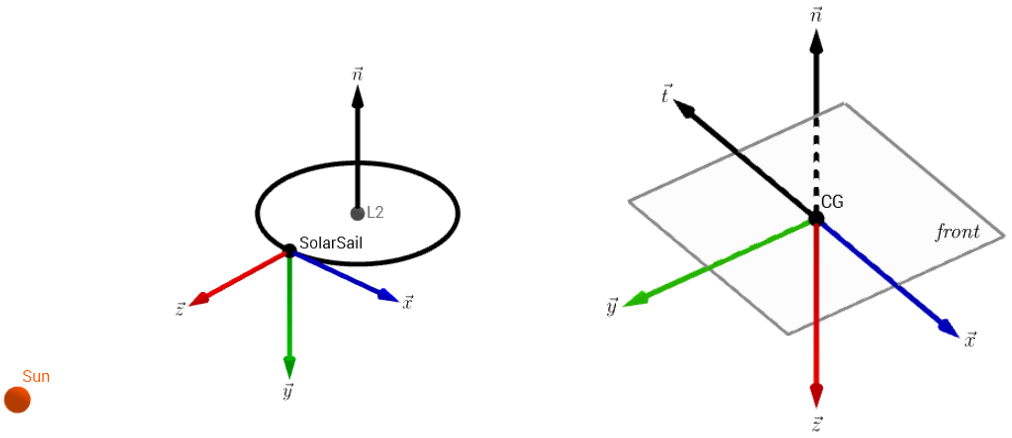

(a) LVLH reference frame

(b) Body reference frame

Figure 2.1: Reference frames

2.2. Quaternions

Quaternions are a set of four parameters used to transform a vector $\vec{u}$ into another vector $\vec{v}$ of different direction and magnitude. Hamilton defined them in 1844 as hyper-complex numbers since them are a complex number extension, being $q = q_1 + iq_2 + jq_3 + kq_4$ with $i^2 = j^2 = k^2 = i\,j\,k = -1$.

In attitude analysis, quaternions represents body attitude in a reference frame with respect to another reference frame. Moreover, attitude propagation is performed efficiently with quaternions since there are only four components instead of nine elements from Direct Cosine Matrix (DCM) and do not have singularities as it happens with Euler angles. For these reasons quaternions will be used for numerical simulations.

Nomenclature and fundamental properties of quaternions used throughout whole project will be discussed below.

2.2.1. Quaternion Nomenclature

Quaternions will be represented by a four row-vector in which the first element q_1 corresponds to scalar notation and the remaining three $q_{2:4}$ to vectorial notation.

$$q = \begin{bmatrix} q_1 \\ q_2 \\ q_3 \\ q_4 \end{bmatrix} = \begin{bmatrix} q_1 \\ q_{2:4} \end{bmatrix} \tag{2.1}$$

Furthermore, quaternions can be written as

$$q_{ab}$$

where q_{ab} defines the vector rotation from reference frame *b* to reference frame *a*. Therefore, vector $\vec{u}$ in reference frame *a* can be defined as the quaternion multiplication between q_{ab} and vector $\vec{u}$ in reference frame *b*, viz.

$$\vec{u_a} = q_{ab}\,\vec{u_b} \tag{2.2}$$

Notation used for quaternion multiplication will be

$$q_{ac} = q_{ab}\,q_{bc} \tag{2.3}$$

2.2.2. Quaternion Operations

There are two different quaternion products that differ only in the sign of the vectorial cross product. Nevertheless, $\bar{q} \otimes q$ has proven to be more useful in attitude analysis.

$$\bar{q} \otimes q = \begin{bmatrix} q_1 q_{\bar{2}:4} + \bar{q}_1 q_{2:4} - q_{\bar{2}:4} \times q_{2:4} \\ \bar{q}_1 q_1 - q_{\bar{2}:4} \dot{q}_{2:4} \end{bmatrix} \tag{2.4}$$

$$\bar{q} \odot q = \begin{bmatrix} q_1 q_{\bar{2}:4} + \bar{q}_1 q_{2:4} + q_{\bar{2}:4} \times q_{2:4} \\ \bar{q}_1 q_1 - q_{\bar{2}:4} \dot{q}_{2:4} \end{bmatrix}$$

Quaternion multiplication is associative and distributive but not commutative, as it happens with matrix multiplication.

$$q \otimes \bar{q} = [q\otimes]\bar{q} = \bar{q} \odot q \tag{2.5}$$
$$q \odot \bar{q} = [q\odot]\bar{q} = \bar{q} \otimes q$$

where $[q\otimes]$ and $[q\odot]$ are

$$[q\otimes] = \begin{bmatrix} q_1 I_3 - [q_{2:4}\times] & q_{2:4} \\ -q_{2:4}^T & q_1 \end{bmatrix} = \begin{bmatrix} \Psi(q) & q \end{bmatrix} \tag{2.6}$$

$$[q\odot] = \begin{bmatrix} q_1 I_3 + [q_{2:4}\times] & q_{2:4} \\ -q_{2:4}^T & q_1 \end{bmatrix} = \begin{bmatrix} \Xi(q) & q \end{bmatrix} \tag{2.7}$$

Where $q_{2:4}\times$ is the matrix cross product defines as

$$q_{2:4}\times = \begin{bmatrix} 0 & -q_4 & q_3 \\ q_4 & 0 & -q_2 \\ -q_3 & q_2 & 0 \end{bmatrix} \tag{2.8}$$

And being matrices Ψ and Ξ respectively

$$\Psi(q) = \begin{bmatrix} q_1 & q_4 & -q_3 \\ -q_4 & q_1 & q_2 \\ q_3 & -q_2 & q_1 \\ -q_2 & -q_3 & -q_4 \end{bmatrix} \tag{2.9}$$

$$\Xi(q) = \begin{bmatrix} q_1 & -q_4 & q_3 \\ q_4 & q_1 & -q_2 \\ -q_3 & q_2 & q_1 \\ -q_2 & -q_3 & -q_4 \end{bmatrix} \tag{2.10}$$

Identity quaternion is defined as

$$I_q = \begin{bmatrix} 1 \\ 0 \\ 0 \\ 0 \end{bmatrix} \tag{2.11}$$

Conjugate of a quaternion is obtained with the change of sign of the vector part.

$$q^* = \begin{bmatrix} q_1 \\ -q_{2:4} \end{bmatrix} \tag{2.12}$$

The product of a quaternion with its conjugate is equal to the square of its norm times the identity quaternion.

$$\|q\|^2 I_q = q^* \otimes q = q \otimes q^* = q^* \odot q = q \odot q^* \tag{2.13}$$

Inverse of a quaternion is defined as the quotient between its conjugate and the square of its norm.

$$q^{-1} = \frac{q^*}{\|q\|^2} \tag{2.14}$$

2.3. Kinematics

Kinematics is a branch of classical mechanics concerned with the geometrically possible motion of a body without consideration of forces or torques

The derivation of the kinematic equation for the quaternion representation is given by

$$\dot{q} = \lim_{\Delta t \to 0} \Delta t_0 \frac{q(t+\Delta t) - q(t)}{\Delta t} \tag{2.15}$$

Rotation from $q(t)$ to $q(t+\Delta t)$ it can be expressed in terms of the exponential of the rotation of a vector,

$$q(t+\Delta t) = \exp\left[\left(\frac{\Delta\vartheta}{2}\right)\otimes\right] q(t) \approx q(t) + \left[\left(\frac{\Delta\vartheta}{2}\right)\otimes\right] q(t) \tag{2.16}$$

Angular rate can be defined as

$$\omega(t) = \lim_{\Delta t \to 0} \frac{\Delta\vartheta}{\Delta t} \tag{2.17}$$

Introducing 2.16 and 2.17 into

$$\dot{q} = \frac{1}{2}\omega(t) \otimes q(t) = \frac{1}{2} q(t) \odot \omega(t) = \frac{1}{2}\Xi(q(t))\ \omega(t) \tag{2.18}$$

2.4. Dynamics

In contrast with kinematics, dynamics analyses the motion of a body in relation to the physical factors that affect them, i.e. mass, force and momentum.

The angular momentum of a body represented on the I frame is

$$H_I^c = \sum_{i=1}^{n} m_i\, r_I^{ic} \times v_I^{ic} = \sum_{i=1}^{n} m_i\, r_I^{ic} \times (\omega_I^{BI} \times r_I^{ic}) = -\sum_{i=1}^{n} m_i [r_I^{ic}\times]\omega_I^{BI} = J_I^c \omega_I^{BI} \tag{2.19}$$

The moment of inertia tensor (MOI) can be defined in the frame in which the vectors r^{ic} are represented. The MOI in a general frame is given by

$$J^c = -\sum_{i=1}^{n} m_i [r^{ic}\times]^2 = \sum_{i=1}^{n} m_i [\|r^{ic}\|]^2 I_3 - r^{ic}(r^{ic})^T \tag{2.20}$$

$$J_B^c = -\sum_{i=1}^{n} m_i [r_I^{ic}\times]^2 = \sum_{i=1}^{n} m_i [\|r_B^{ic}\|]^2 I_3 - r_B^{ic}(r_B^{ic})^T$$

The angular momentum in the body frame is given by the dot product between MOI tensor and angular velocity,

$$H_B^c = J_B^c \omega_B^{BI} \tag{2.21}$$

Therefore, angular velocity it can be expressed in body frame as

$$\omega_B^{BI} = (J_B^c)^{-1} H_B^c \tag{2.22}$$

The first derivative of angular momentum is given by

$$\dot{H}_B^c = L_B^c - \omega_B^{BI} \times H_B^c \tag{2.23}$$

From 2.19, 2.21 and 2.23 it can be obtained Euler's rotational equation, i.e. the first derivative of angular velocity in body frame

$$\dot{\omega_B^c} = (J_B^c)^{-1} \left[L_B^c - \omega_B^{BI} \times (J_B^c \omega_B^{BI}) \right] \tag{2.24}$$

where J_B^c is the MOI tensor, L_B^c is the total torque and ω_B^{BI} is the angular body rate.

L_B^c is composed by both undesirable disturbance torques and torques deliberately applied for control. As a simplification it will be considered solely the torque generated by SRP which can be defined as,

$$L_{SRP} = F_{SRP} \cdot r \tag{2.25}$$

Where F_{SRP} is the SRP force and r is CoP-CoM offset. The torque generated by actuators is discussed in section 4.1..

CHAPTER 3. ATTITUDE DETERMINATION SUBSYSTEM

3.1. Sensors

To guarantee the correct development of the mission and to successfully realize the scientific experiments, the orientation and position of the solar sail must be determined. The Attitude Determination and Control Subsystem (ADCS) is the responsible for this task. Due to the dynamics of the satellite it is a particularly complicated task and the accuracy of the sensors and algorithms will condition the performance of the subsystem.
The sensors used are listed below in Table 3.1 and their detailed technical specifications can be found in the appendices.

Model	Sensor	Description
ADXRS290	Coriolis Vibratory Gyroscope	CVG for pitch and roll angular rate measurements.
ADXRS453	Coriolis Vibratory Gyroscope	CVG for yaw angular rate measurements.
nanoSSOC-A90	Analog Sun Sensor	Incident light measurement for azimuth and elevation angles.
IIS2DH	MEM Accelerometer	Three axis linear accelerometer for inertial measurements.

Table 3.1: Attitude determination sensors

3.1.1. Gyroscopes

Gyroscopes are used for angular rate measurements and attitude integration between sensor measurements. The output is about the body axes, but the measurements are w.r.t. the inertial frame. In function of the physical mechanism can be classified as spinning-mass gyros, optical gyros or Coriolis Vibratory Gyros (CVGs).

- Spining-mass gyros are based on the law of conservation of angular momentum which states that angular momentum is constant, in both magnitude and direction, if the external torque is zero.
- Optical gyros are based on Sagnac effect. This phenomenon can be explained as a light source emitting two beams of light that travel identical paths but in opposite direction. If the system is rotating, one of the beams must travel a greater distance than the opposite. The difference in travel times is detected as a phase shift and thus as angular velocity. Since they do not contain moving parts are not affected by mechanical wear or drifting.
- CVGs operate under Coriolis effect. CVG's contain a mass connected to an outer housing by a set of springs. Rotation of the system is detected by differential capac-

itance as the mass is pushed by Coriolis force. Thus angular velocity can be measured. These types of gyroscopes are MEMS (Micro-machined Electro-Mechanical Systems) which have very low mass and low power requirements.

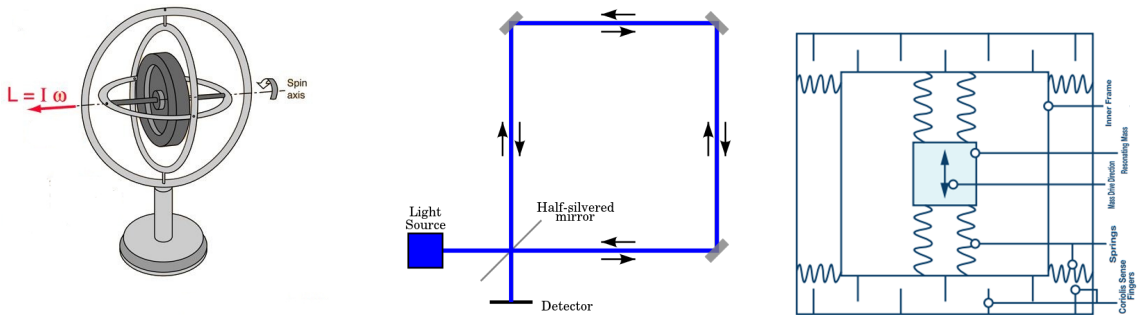

(a) Spining-mass gyro (b) Optical gyro (c) Coriolis vibratory gyro

Figure 3.1: Gyroscopes

3.1.2. Sun Sensors

Sun sensors are photo-diodes used to get attitude information. Can be classified as analog sun sensors or digital sun sensors. The output of photocells is an electric current directly proportional to the intensity of the light. In particular, the output current varies with a cosine relationship to the incident angle with sun. Sun sensors have to be calibrated to compensate the effect of albedo and glint.

3.1.3. Accelerometers

Accelerometers measure the acceleration of a mass relative to their base. The principle of operation is based on Newton's second law, which states that the acceleration experienced by a mass is dependent upon the net force acting. They can be used for inertial measurements of velocity and position, but since they are continually integrating acceleration w.r.t time, measurements errors are accumulated over time leading to 'drift' or secular errors.

3.2. Attitude determination algorithm

Attitude determination (AD) can be classified into two cathegories: static AD and dynamic AD. The first consider that all measurements are taken at the same time or close enough in time that spacecraft motion between the measurements can be ignored. Thus the problem becomes up of solving the geometry of the measurements. The second type consider that measurements are taken over the time. In this case, attitude measurements and angular rate measurements need to be blended together.

For a three dimensional orientation measurement (three-degree of freedom problem) is needed a minimum of two observation vectors each with two independent degrees of freedom. Thus, AD problem is always over-determined.

Attitude observations are presented as unit vectors since the length of the vector has no relevant information to AD. These observations can be modelled as the real value of the measurement plus an error due to sensor noise and bias.

$$\vec{b} = \vec{b_0} + \vec{\delta b} \tag{3.1}$$

AD problem consist on finding a rotation matrix A (DCM) that transform measurements vectors from spacecraft body frame b_i to a reference frame r_i. Wahba formulated a general criterion to find the orthogonal matrix A that minimizes the loss function

$$L(A) = \frac{1}{2}\sum_{i=1}^{N} a_i \|b_i - Ar_i\|^2 = \lambda_0 - tr(AB^T) \tag{3.2}$$

where b_i are the measurement vectors in spacecraft body frame, r_i are the corresponding vectors in reference frame and a_i are the quality weights between the measurements. Values of λ_0 and B matrix are given by

$$\lambda_0 = \sum_{i=1}^{N} a_i \qquad B = \sum_{i=1}^{N} a_i b_i r_i^T \tag{3.3}$$

Loss function is showed in Fig. 3.2 as the error of the common least squares curve fitting problem.

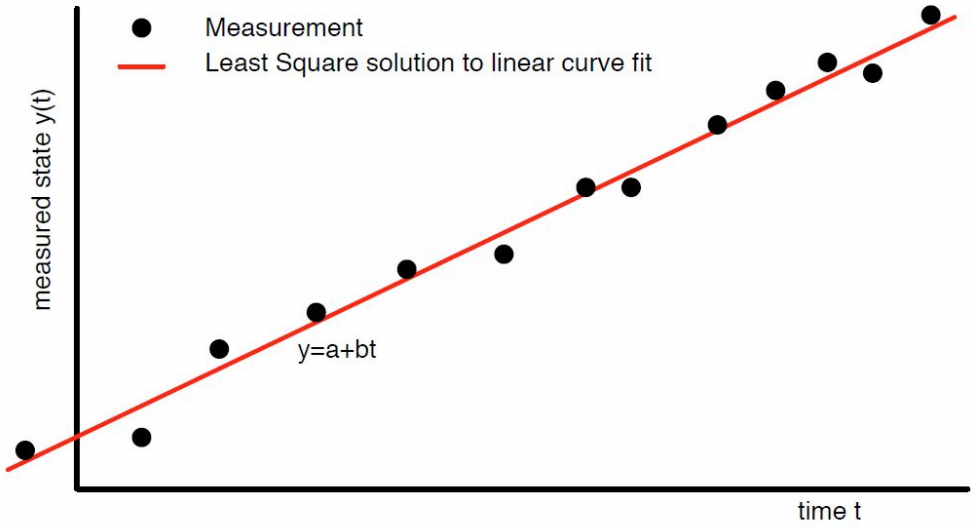

Figure 3.2: Least square curve fitting problem

As discussed in section 2.2., rotation matrix can be represented as a quaternion $\vec{q}$. Thus Eq. 3.2 can be rewritten as

$$L(A(q)) = \lambda_0 - \vec{q}^T K \vec{q} \tag{3.4}$$

The REQUEST algorithm defines the K matrix for each instant t_{k+1} as

$$\delta K_{k+1} = \frac{1}{a_{k+a}} \begin{bmatrix} \delta S_{k+1} - \sigma_{k+1} I_{3x3} & \delta\vec{\tau}_{k+1} \\ \delta\vec{\tau}_{k+1}^T & \delta\sigma_{k+1} \end{bmatrix} \tag{3.5}$$

where

$$\delta B_{k+1} = a_{k+1}\, \vec{b}_{k+1}\, \vec{r}_{k+1}^T \tag{3.6}$$

$$\delta S_{k+1} = \delta B_{k+1} + \delta B_{k+1}^T \tag{3.7}$$

$$\delta\vec{\tau}_{k+1} = a_{k+1}\, \vec{b}_{k+1}^T\, \vec{r}_{k+1} \tag{3.8}$$

$$\delta\sigma_{k+1} = tr(\delta B_{k+1}) \tag{3.9}$$

As mentioned above, dynamic AD consider spacecraft motion between measurements. To solve the dynamic problem it is proposed Optimal REQUEST algorithm which follow Kalman filter strategy. The propagation of estimate measurements, i.e. K matrix, and the uncertainty propagation of the estimation process, i.e. P matrix, is carried out in parallel.

$$K_{k+1/k} = \phi_k\, K_{k/k}\, \phi_k^T \tag{3.10}$$

$$P_{k+1/k} = \phi_k\, P_{k/k}\, \phi_k^T + Q_k \tag{3.11}$$

where the subscript $k+1/k$ refers to the predicted estimate and ϕ_k is the rotation matrix due to angular rate at instant t_k.

$$\phi_k = \exp(\Omega_k\, \Delta t) \tag{3.12}$$

$$\Omega_k = \begin{bmatrix} 0 & \omega_z & -\omega_y & \omega_x \\ -\omega_z & 0 & \omega_x & \omega_y \\ \omega_y & -\omega_x & 0 & \omega_z \\ -\omega_x & -\omega_x & -\omega_z & 0 \end{bmatrix} \tag{3.13}$$

The update of the estimate, denoted by subscript $k+1/k+1$, is formulated as linear combination of the predicted estimate, indicated with subscript $k+1/k$, and the new observation, denoted by subscript $k+1$.

$$K_{k+1/k+1} = (1 - \rho_{k+1}^*)\frac{m_k}{m_{k+1}} K_{k+1/k} + \rho_{k+1}^* \frac{\delta m_{k+1}}{m_{k+1}} \delta K_{k+1} \tag{3.14}$$

$$P_{k+1/k+1} = \left[(1 - \rho_{k+1}^*)\frac{m_k}{m_{k+1}}\right]^2 P_{k+1/k} + \left[\rho_{k+1}^* \frac{\delta m_{k+1}}{m_{k+1}}\right]^2 R_{k+1} \tag{3.15}$$

where ρ_{k+1} is the optimal filter gain, R_{k+1} represents the noise model of the measurements, δm_{k+1} is a positive scalar weight and m_{k+1} is obtained recursively from

$$m_{k+1} = (1 - \rho_{k+1}^*) m_k + \rho_{k+1}^* \delta m_{k+1} \tag{3.16}$$

being $m_0 = \delta m_0$.

The optimal filter gain is computed in order to minimize the estimation uncertainty. Thus, is that which yields an optimal blending of the a priori estimate $K_{k+1/k}$ and the new observation δk_{k+1}.

$$\rho^*_{k+1} = \frac{m_k^2\, tr(P_{k+1/k})}{m_k^2\, tr(P_{k+1/k}) + \delta m_{k+1}^2\, tr(R_{k+1})} \tag{3.17}$$

When K matrix is determined, the quaternion that estimates the spacecraft attitude ($\vec{q}^*$) is the eigenvector of the largest eigenvalue (λ_{max}). This could imply a high consumption process. The Quaternion Estimator (QUEST) algorithm provides a simple model to compute the estimated quaternion as

$$\vec{q}^* = \frac{1}{\sqrt{\gamma^2 + |\vec{x}|^2}} \begin{bmatrix} \gamma \\ \vec{x} \end{bmatrix} \tag{3.18}$$

where

$$\gamma = adj([\lambda_{max} + tr(B)]I_{3x3} - B - B^T)\vec{\tau} \tag{3.19}$$

$$\vec{x} = det([\lambda_{max} + tr(B)]I_{3x3} - B - B^T) \tag{3.20}$$

Finally, with Newton-Raphson iteration of the characteristic equation, the largest eigenvalue of K matrix is obtained.

$$det([\lambda_{max} I_{3x3} - K] = (\lambda_{max} + tr(B))\gamma - \vec{\tau}^T \vec{x} = 0 \tag{3.21}$$

CHAPTER 4. ATTITUDE CONTROL SUBSYSTEM

4.1. Actuators

Control subsystem must be reliable and lightweight, so the use of thin-film RCDs (Reflectivity Control Devices) is proposed. These devices are electro-active materials that change its surface reflectivity as a function of applied electric potential. In this project, the space qualified, Li-based and solid-state system EclipseVEECD (Variable Emittance Electro-Chromic Device) is chosen as the attitude control actuator.

The application of small voltage on the VEECD leads to movements of $Li^+ + e^-$ pairs between ion-storage (IS) and electrochromic (EC) layers through solid fast ion conductor (EL), changing the optical properties of the active element. Figures 4.1(a) and 4.1(b) show the structure and the active element of VEECD respectively.

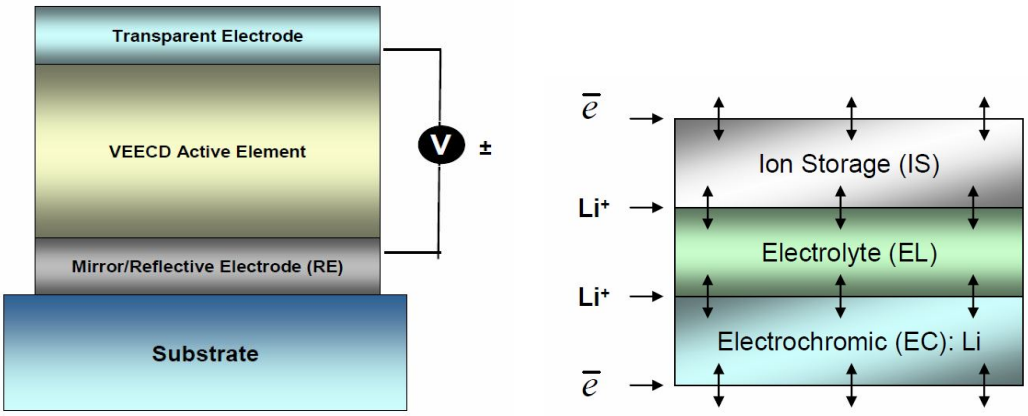

(a) VEECD Schematic

(b) VEECD Active element

Figure 4.1: Variable Emittance Electro-Chromic Device

Although these devices are commonly used for thermal control, investigations carried out by leading space agencies such as NASA, ESA and JAXA propose the use of RCDs as actuators for solar sails.
Attitude control method proposed is based on CoM-CoP distance. By modifying the surface reflectivity of the solar sail, the SRP acting on the surface can be modulated. Therefore the total body force and torque, which depends on the CoM to CoP vector, can be controlled without using mechanical systems or thrusters.

Since RCD actuators are placed in X-Y plane. Then can only deliver a control torque with two components for controlling three rotational degrees of freedom. Both components depend on the distribution and activation state of the RCD elements, thus they cannot be controlled independently. RCD is restricted to operate at two discrete reflectivity states, either *coloured* (high-emittance and low-reflectance) or *bleached* (low-emittance and high-reflectance). The SRP torque generated by each cell n of area $A_n = \Delta x \Delta y$ and distance $(r_{x,n}, r_{y,n})$ from CoM is

$$\begin{bmatrix} T_{x,n} & T_{y,n} & T_{z,n} \end{bmatrix} = SRP_n \cdot r_{x,y,z,n} \tag{4.1}$$

where distance between cell and CoM in Z axis is $r_{z,n} = 0$ and then $T_z = 0$. Generated

torque from Eq. 4.1 is function of angle α (i.e. light incidence angle), cell area, cell optical properties (i.e. absorption a, emissivity ε and reflectance ρ) and CoP-CoM distance. It should be noted that torque magnitude will vary with spacecraft attitude due to α changes.

For the analysis it has been considered four RCD elements of $42.84cm^2$ of area placed on each corner of the solar sail surface. Fig. 4.2 shows in detail the RCD position with respect to the corner. The distances between the CoP of each cell and CoM of the solar sail are detailed in Table 4.1.

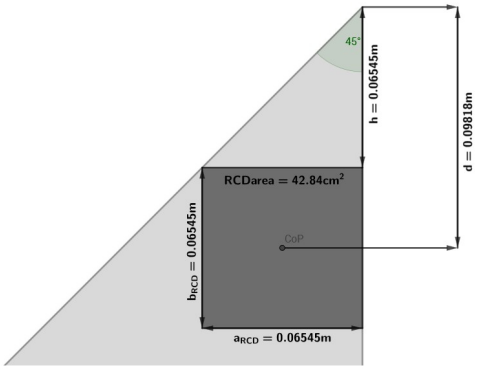

Figure 4.2: Detail of RCD_n placement

Axis	CoP - CoM distance (m)			
	RCD_1	RCD_2	RCD_3	RCD_4
r_x	1.5484	1.4830	-1.5484	-1.4830
r_y	1.4830	-1.5484	-1.4830	1.5484
r_z	0	0	0	0

Table 4.1: Torque arm

As it can be seen from the results of Table 4.1, it has been neglected CoP-CoM offset in Z axis. Moreover, the active element surface is assumed as a perfect reflecting mirror (specular reflection only) omitting all other optical interactions such as absorption, re-emission or diffusely reflection. Therefore, the optical properties of each RCD are $\rho_{on} = 1$ for *bleached state* or $\rho_{off} = 0$ for *coloured* state. Tables 4.2 and 4.3 show the generated torque for the *bleached* and *coloured* state respectively.

Axis	RCD torque ($\times 10^{-8}$)			
	1	2	3	4
x	5.8888	5.6399	-5.8888	-5.6399
y	5.6399	-5.8888	-5.6399	5.8888
z	0	0	0	0

Table 4.2: Torque generated per RCD operating at bleached state ($\rho_{RCDon} = 1$)

Axis	RCD torque ($\times 10^{-8}$)			
	1	2	3	4
x	2.9444	2.8199	-2.9444	-2.8199
y	2.8199	-2.9444	-2.8199	2.9444
z	0	0	0	0

Table 4.3: Torque generated per RCD operating at coloured state ($\rho_{RCDoff} = 0$)

The number of possible reflectivity combinations using four two-state RCD's is 8 as shown in Fig. 4.3. It should be noted that every symmetric combination does not create torque since the generated force by opposite elements cancel out. Table 4.4 show the possible combinations as function of each RCD state.

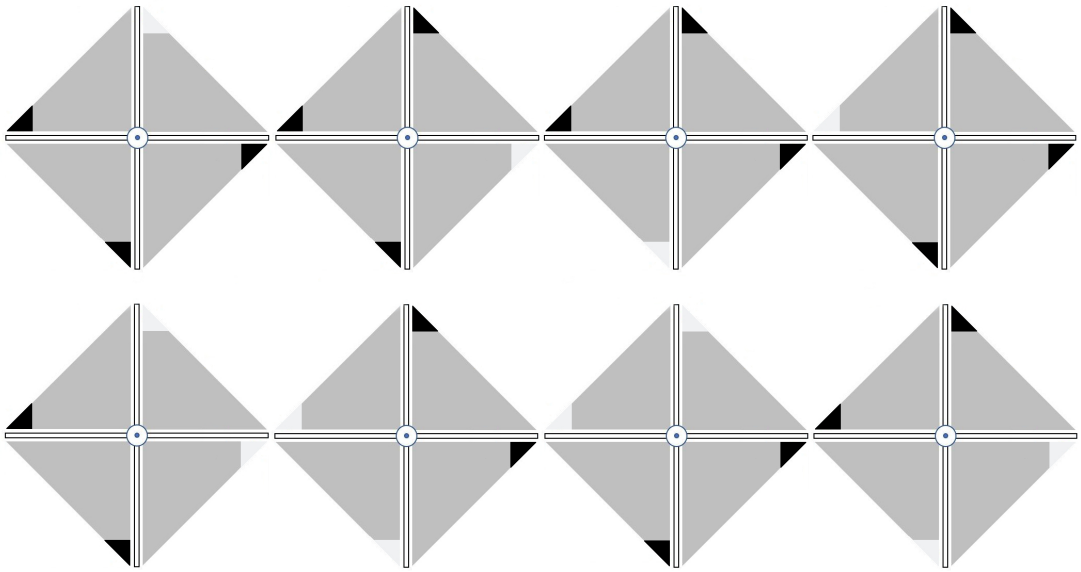

Figure 4.3: Possible reflectivity combinations

D	Case							
	1	2	3	4	5	6	7	8
RCD_1	1	0	0	0	1	0	0	1
RCD_2	0	1	0	0	1	1	0	0
RCD_3	0	0	1	0	0	1	1	0
RCD_4	0	0	0	1	0	0	1	1

Table 4.4: Possible reflectivity combinations

Knowing the generated torque by each of the RCDs in both states of reflectivity, the net torque vectors produced for each possible combination can be determined.

Axis	Torque for each RCD combination ($\times 10^{-8} Nm$)							
	1	2	3	4	5	6	7	8
x	2,9444	2.8199	-2,9444	-2.8199	5.7643	-0.1244	-5.7643	0.1244
y	2.8199	-2,9444	-2.8199	2,9444	-0.1244	-5.7643	0.1244	5.7643
z	0	0	0	0	0	0	0	0

Table 4.5: Torque vector generated for each reflectivity combination

4.2. Control algorithm

This is a case of regulation control, where the attitude of the satellite is brought to some fixed orientation while the spacecraft's angular velocity is reduced to zero. To determine the attitude of the satellite, a quaternion-based approach is used. In this case, the quaternion relates the orientation of the spacecraft's body frame with respect to the orbital frame. The objective of the nominal controller is to align the spacecraft's Z axis with the Z axis of the orbital frame, which is defined to point towards the Sun.

The motion of the spacecraft in orbit is governed by the quaternion attitude kinematic equation 2.18 and the Euler's rigid body equation 2.24:

The goal of the nominal controller is to drive the current quaternion q to some commanded quaternion q_c. The error quaternion between the current and the desired quaternion is given by,

$$\delta q = \begin{bmatrix} \delta q_1 \\ \delta q_{2:4} \end{bmatrix} = q \otimes q_c^{-1} \tag{4.2}$$

Substituting 4.2 into 2.18, it is obtained the time derivative of the error quaternion,

$$\delta \dot{q} = \frac{1}{2} \Xi(\delta q) \dot{\omega} \tag{4.3}$$

which can be divided into the vector and scalar parts,

$$\dot{\delta q_{2:4}} = \frac{1}{2} \delta q_{2:4} \times \omega + \frac{1}{2} \delta q_1 \omega \tag{4.4}$$

$$\dot{\delta q_1} = -\frac{1}{2} \delta q_{2:4}^T \omega$$

The goal of the nominal controller is to drive the actual quaternion to the desired attitude while tumbling motion towards zero angular velocity. This means, bringing the error quaternion to the identity quaternion [1, 0, 0, 0] and ω to zero.
For this mode, a linear PD quaternion-based feedback control is proposed.

PD controllers are based on feedback mechanism which uses information from measurements. Proportional action depends on the present error and can be adjusted by proportional gain k_p. Increasing k_p results in a large change in the output so the response becomes faster with lower steady state error but more oscillatory. Derivative action depends on the slope of the error over the time and can be adjusted by derivative gain k_d. This term slows the rate of change of the controller output and has the effect of increasing the stability of the system reducing the overshoot and improving transient response.
Thus, the control torque L_c is given by the following control law,

$$L_c = -k_p \, sign(\delta q_1) \, \delta q_{2:4} - k_d \, \omega \tag{4.5}$$

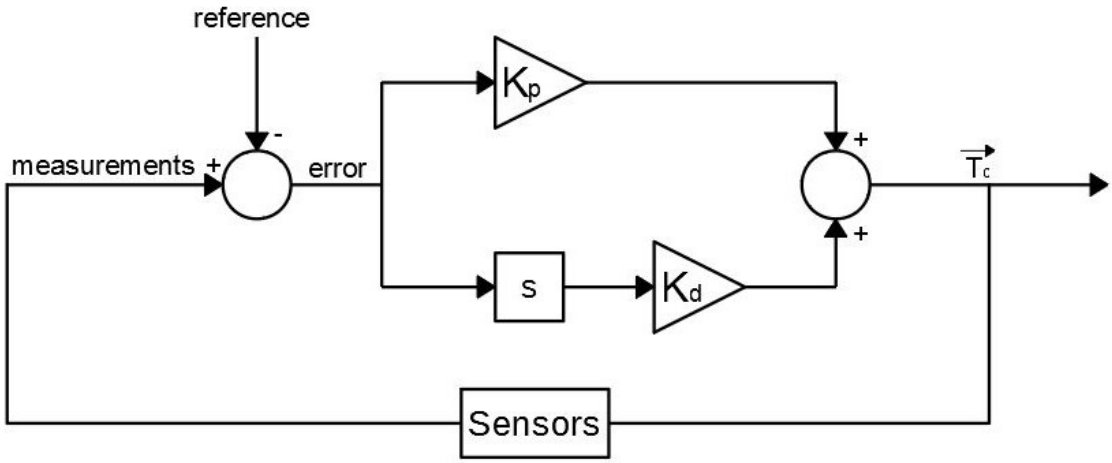

Figure 4.4: PD block diagram

Note that when the vector quaternion term $\delta q_{2:4}$ and ω are [0, 0, 0] respectively, then the control torque vanishes. Furthermore, if $\delta q_1 < 0$ a positive feedback term is introduced, which provides a shorter path to reach the desired equilibrium point.

Control law gains must be defined empirically such that the control torque matches the maximum torque achievable by RCDs. As it has been seen in previous section, there are a set of reflectivity combinations that provide a finite number of possible torques depending on the satellite's attitude. The best achievable torque $(T_x, T_y, 0)$ is found by scanning the reflectivity combinations for the closest match with reference torque (L_x, L_y, L_z).

CHAPTER 5. ATTITUDE DETERMINATION AND CONTROL SYSTEM ANALYSIS

5.1. Theoretical analysis

To analyze theoretically the stability of the control subsystem, the Lyapunov's direct method and LaSalle's invariance theorem are used.

Lyapunov's direct method states that if the total energy of a mechanical system is continuously dissipated then the system must eventually settle down to an equilibrium point x_e and therefore it is stable. Furthermore, asymptotic stability means that states started close to the x_e converge to x_e as time goes to infinity. If asymptotic stability holds for any initial state, the system is said to be globally asymptotically stable.

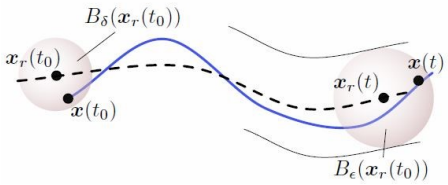

(a) Lyapunov stability

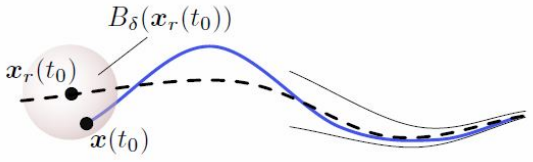

(b) Asymptotic stability

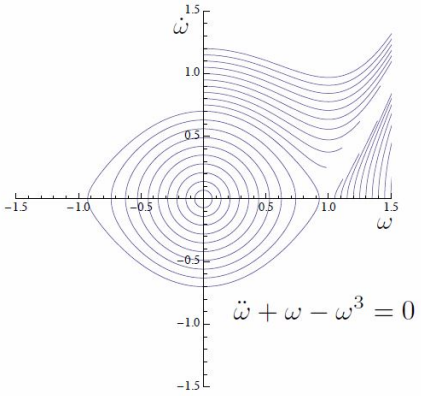

(c) Global stability

Figure 5.1: Stability definitions

The direct method procedure is to generate a scalar *'energy-like'* function for the dynamic system and study its time variation. Lyapunov function is a scalar function which satisfies:

$$V(x_e) = 0$$

$$V(x) > 0 \qquad for\ x \neq x_e$$

$$\dot{V}(x) \leq 0$$

Substituting control law Eq. 4.5 into Euler's rotational Eq. 2.24 gives the closed-loop system

$$\dot{\omega}_B^c = -(J_B^c)^{-1}\left[k_p sign(\delta q_1)\delta q_{2:4} - k_d\omega + \omega_B^{BI} \times (J_B^c \omega_B^{BI})\right] \tag{5.1}$$

From Eq. 5.1 it can be seen that equilibrium point x_e is $[\delta q_{2:4} \quad \omega] = 0$

The Lyapunov candidate function chosen for this analysts is

$$V = \frac{1}{4}\omega^T[J]\omega + \frac{1}{2}k_p\delta q_{2:4}^T \cdot \delta q_{2:4} + k_p(1-\delta q_1)^2 \tag{5.2}$$

Since $[J]$ is a positive definite matrix and k_p is a positive gain, the Lyapunov candidate function is positive definite. The derivative of V respect to time gives,

$$\dot{V} = \frac{1}{2}\omega^T[J]\dot{\omega} + k_p\delta q_{2:4}^T \cdot \dot{\delta q_{2:4}} - k_p(1-\delta q_1)\dot{\delta q_1} \tag{5.3}$$

Substituting 4.4 and 5.1 into 5.3 and doing some algebra gives,

$$\dot{V} = -\frac{1}{2}(\omega^T\delta q_{2:4})[k_p + k_p\delta q_1 - k_p(1+\delta q_1)] - \frac{1}{2}k_d\omega^T\omega = -\frac{1}{2}k_d\omega^T\omega \leq 0 \tag{5.4}$$

Above equation shows that $\dot{V} = 0$ when $\omega = 0$ whereas $\delta q_{2:4}$ can be arbitrary, so Lyapunov function is said to be negative semi-definite (assuming $k_d > 0$). Thus, it can not be guaranteed asymptotic stability.
LaSalle's invariance theorem help to draw conclusions on asymptotic stability. Eq. 5.1 shows that asymptotic stability can only be achieved if $\omega = 0$ and $\lim_{t\to\infty}\delta q_{2:4} = 0$. Thus, closed loop system is globally asymptotically stable.

Theoretical analysis conclude that control subsystem can detumble and reorient the spacecraft to desired attitude from any initial orientation and angular rate.

5.2. Numerical analysis

To verify the conclusions of the previous theoretical analysis, a numerical simulation of the system is performed in MATLAB. The MATLAB scripts used to perform these simulations are enclosed in section A of ANNEX. These codes aim to simulate rigid-body dynamics of the solar sail using quaternions for attitude representation.

5.2.1. Assumptions and limitations

The list below presents the different assumptions and aspects considered to perform the analysis.

- The solar sail is located at the farthest point of the L2 orbit throughout the simulation.
- Disturbance forces are neglected.
- The solar sail ia a rigid body.
- The solar sail CoM is coincident with the GC.
- The solar sail mass distribution is homogeneous.
- The solar sail can be modelled as a rectangular parallelepiped.

- Ideal sensors and actuators are considered.
- The solar sail surface is considered Lambertian.
- The RCDs are restricted to operate at two discrete reflectivity states.
- The RCDs are assumed as perfectly reflecting mirrors.
- The initial relative attitude is random.
- The initial angular rate is zero.

5.2.2. Analysis description

The solar sail can be modelled as a rigid rectangular parallelepiped with homogeneous mass distribution. Four RCDs are placed in each border of the sail's front surface as shown in Fig. 4.3. The physical and optical parameters for the solar sail and the actuators are detailed in tables 5.1 and 5.2.

Parameter	Value
Sail size	$3.16m \times 3.16m \times 7.5 \times 10^{-6}m$
Sail area	$10m^2$
Sail mass	$540.77g$
ADCS mass	$5.24g$
CoM	$[0\ \ 0\ \ 0]cm$
RCD per side	4
RCD size	$6.55cm \times 6.55cm$
RCD area	$42.84cm^2$

Table 5.1: Solar sail parameters used in simulation

Parameter	Sail	RCD 'on'	RCD 'off'
a	0.08	0	0
ε_f	0.02	0	0.02
ε_b	0.17	0.17	0.17
ρ_s	0.92	1	0
ρ_d	0	0	0
B_f	2/3	2/3	2/3
B_b	2/3	2/3	2/3

Table 5.2: Optical parameters used in simulation

Using the data from above tables, the MOI matrix of the solar sail can be defined as

$$J = \int \rho(x,y,z) \begin{bmatrix} y^2+z^2 & -xy & -xz \\ -xy & z^2+x^2 & -yz \\ -xz & -yz & x^2+y^2 \end{bmatrix} = \tag{5.5}$$

$$= \begin{bmatrix} \frac{1}{12}(l_y^2+l_z^2)M & 0 & 0 \\ 0 & \frac{1}{12}(l_x^2+l_z^2)M & 0 \\ 0 & 0 & \frac{1}{12}(l_x^2+l_y^2)M \end{bmatrix} = \begin{bmatrix} 4.5064 & 0 & 0 \\ 0 & 4.5064 & 0 \\ 0 & 0 & 9.0128 \end{bmatrix}$$

The rigid-body attitude dynamics of the solar sail is described using quaternion kinematics equation and Euler's equation. Kinematics Eq. 2.18 represents the first derivative of the attitude quaternion due to angular velocity and Euler's Eq. 2.24 describe the change of angular velocity due to an external torque. Since external disturbance torques are neglected, the only torque acting on the system will be the generated by the RCDs.

With the optical parameters of the actuators, and knowing the angle between sail's normal and sun-line vectors, SRP force perceived in CoP of each actuator for both reflectivity states can be determined. The distance of each device with respect to the CoM does not vary and therefore the generated torque can be easily known. From table 4.4 is determined the state of each RCD for each reflectivity combination and thus the torque generated in every case can be computed.

According to section 4.2., a linear PD control law is applied to obtain the reference torque needed to achieve the desired attitude while reducing angular rate to zero (detumbling). By comparing the reference torque with the generated by each of RCDs reflectivity combinations, the torque acting on the system can be found.

5.2.3. Analysis results

In order to evaluate the correct performance of the attitude control system, solar sail's attitude is presented in its Euler angle and Quaternion representations (Fig. 5.2 and Fig. 5.3 respectively). Moreover, Fig. 5.4 shows the relative angular rates, and Fig. 5.5 presents the reference and RCD's generated torque with respect to time.

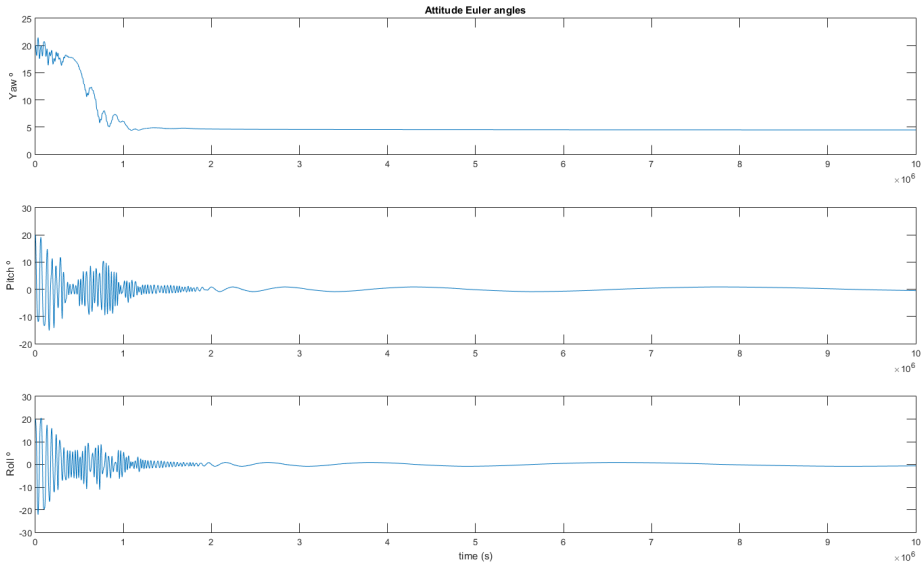

Figure 5.2: Solar sail attitude in Euler angles representation in °

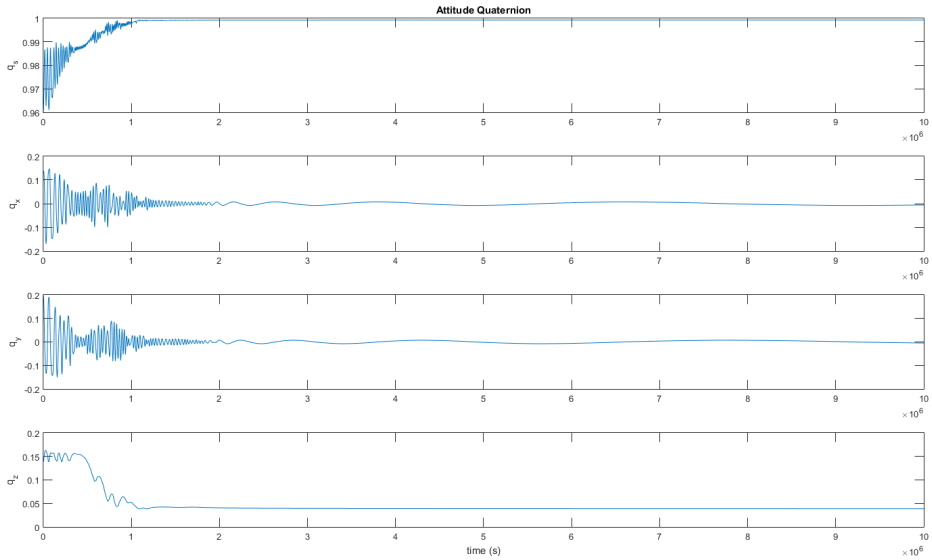

Figure 5.3: Solar sail attitude in Quaternion representation

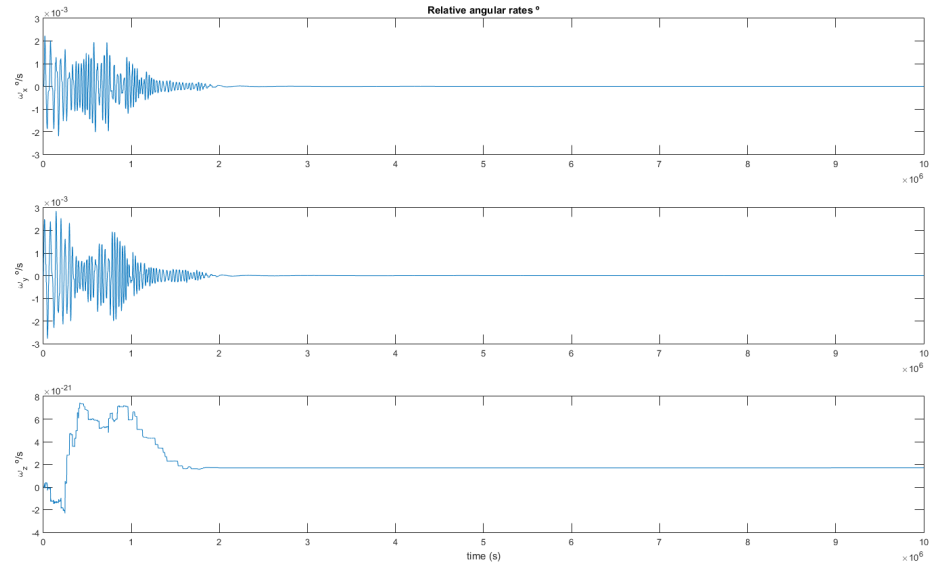

Figure 5.4: Angular rates in ^{o}/s

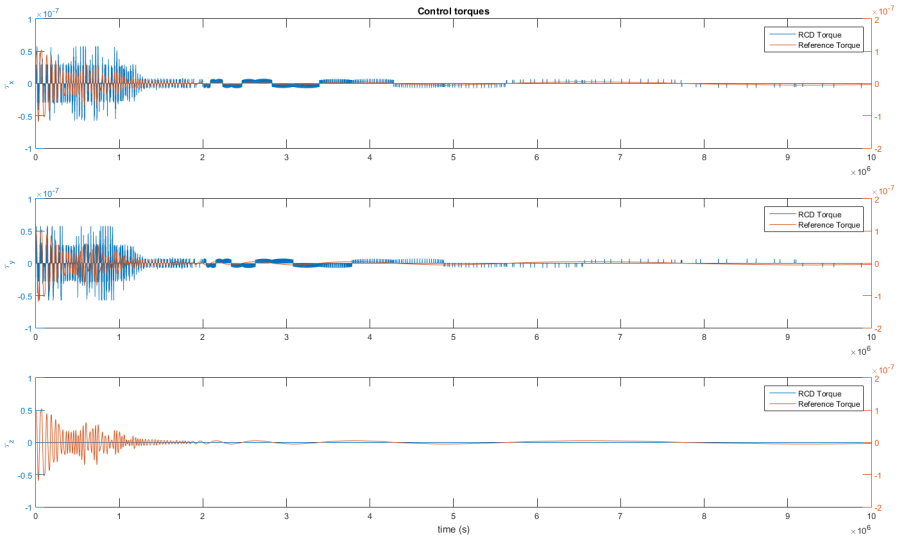

Figure 5.5: Reference and RCDs net torque in Nm

Fig. 5.2 shows the relative attitude in Euler angle representation. It can be seen how the attitude oscillates in pitch and roll axes (those axes in which control is applied) and converges until stabilizing around zero degrees, indicating the alignment of body and LVLH reference frames. These results are corroborated by those obtained in Fig. 5.3, that show the relative attitude in quaternion representation. In this case, it can be seen an oscillating behaviour converging to the identity quaternion $[1\ 0\ 0\ 0]$, which again indicate the alignment of reference frames. Since the LVLH reference frame has been defined such that Z axis is pointing towards the sun, the alignment of the body and LVLH reference frames means that the sail's normal vector is coincident with the sun-line vector.

Fig. 5.4 present the relative angular rate for each axis. In the Z axis the angular rate remains at 0^o/s because no control torque is applied to this axis. The X and Y axes, which have initial angular velocity equal to zero, oscillate due to control torques until stabilize at 0^o/s. This indicates that the derivative part of the PD control law is capable of detumbling the solar sail for low angular velocities (order of magnitude $10^{-3}\ ^o/s$). On the other hand, the simulations which have introduced higher initial angular velocities show an unstable behaviour of the system, maybe because the torque generated by the actuators is very weak. Some possible solutions to this issue are discussed in 7, such as increasing RCDs size or solar sail surface (since CoP - CoM offset would be greater) to increase the torque.

Fig. 5.5 shows the generated torque by RCDs (marked in blue) and the reference torque determined by control law (marked in red). It should be noted that control law gains are tuned such that the maximum reference torque match the maximum torque achievable by RCDs. As it has been said before, the RCDs actuators can only deliver torque in the X-Y axes, thus in the Z axis there is no attitude control.

In conclusion, starting from initial random attitude and zero angular velocity, above graphs show that control subsystem is capable of align solar sail's body axes with the LVLH reference frame, i.e. align surface normal vector with sun-line vector. The simulation has been carried out multiple times to verify the stability of the system regardless of the initial attitude. The results conclude that the ADCSS is globally asymptotically stable.

CONCLUSIONS AND FURTHER WORK

5.3. Conclusions

The aim of this final degree thesis has been to analyse the Guidance, Navigation and Control strategy for a solar sail of $10m^2$. For the position determination has been chosen an IMU using a combination of a three-axial accelerometer and two gyroscopes. Therefore, the position knowledge does not depend on GPS or star trackers, which have higher mass and power consumption requirements. To deal with the integration errors, the measurements will be corrected periodically with the eclipse readings.

The attitude determination will be done by applying the recursive estimation algorithm Optimal-REQUEST, which has as input parameters the sun sensors data as attitude measurements, the gyroscopes data to consider the case where the body rotates between measurements and the sensor noise models.

To guarantee the Sun pointing, the ADCS is required to be asymptotically stable for any initial condition. As actuators has been proposed the use of four RCDs, placed in each of the corners of the FemtoSail. Thus, the distance of the CoP of each device with respect to the CoM (and therefore the generated torque) are the highest possible. Depending on the state of each device, there is a finite number of possible net torques in pitch and roll axes. It has been implemented a lineal PD control law, whose aim is reach a desired attitude while reducing the angular rate to zero. The output of the control law is a reference torque used to choose, from the possible combinations of RCDs states, the optimal net torque to perform the maneuver.

The theoretical analysis by Lyapunov's direct method and LaSalle's invariance theorem conclude that the system is globally asymptotically stable. This conclusion is corroborated by the numerical analysis, which shows, for any initial attitude, the convergence to the identity quaternion and an angular rate of 0^o/s on each axis.

It is necessary to emphasize that the time required to reach the Sun pointing varies according to initial attitude. That is, the greater the deviation between sail's normal and Sun-line vector, the longer the time required. In any case, the required time is very high (order of magnitude $10^6 s$ since the generated torques are very weak (order of magnitude $10^{-8} Nm$). On the other hand, for initial angular rates greater than zero, the subsystem has an unstable behaviour because it is unable to compensate the rotation of the FemtoSail.

5.4. Further work

The simulations that have been carried out in this thesis have taken into account a set of limitations and assumptions in order to simplify the analysis. Therefore the analysis have not yet concluded.

The behaviour of the FemtoSail should be evaluated in each of the points of the Lagrangian L2 orbit proposed for the mission. By doing this, an eclipse model could be implemented to study the effect on the determination and control subsystem.

Further investigation in the three-axis control methods with reflectivity control devices must be carried out, either by tilting RCDs or combining it with other control methods such as control vanes or gimbaled masses method.

The incidence of the initial angular rate on the stability of the system has not been studied. Thus, the limit of stability and possible solutions should be investigated.

Finally, the attitude determination should be implemented on the numerical analysis taking into account the bias and drift of the sensors. In addition, the reaction time of the RCDs and the optical properties curve should be considered.

BIBLIOGRAPHY

[1] McInnes, Colin Robert. “Solar Radiation Pressure”. *Solar Sailing Technology, Dynamics and Mission Applications*. (Springer-Praxis. London. 1999): 32–55.

[2] Markley, F. Landis, Crassidis, John L. “Matrices, Vectors, Frames, Transforms”. *Fundamentals of Spacecraft Attitude Determination and Control*. (Springer-Verlag. New York. 2014): 17–65.

[3] Markley, F. Landis, Crassidis, John L. “Attitude Kinematics and Dynamics”. *Fundamentals of Spacecraft Attitude Determination and Control*. (Springer-Verlag. New York. 2014): 67–122.

[4] Paliszek, Michael, Razin, Yosef, Pajer, Gary, Mueller, Joseph, Thomas, Stephanie. “Kinematics”. *Spacecraft Attitude and Orbit Control, Volume 1: A Systems Approach*. (Princeton Satellite Systems. Plainsboro NJ. 2012): 41–51.

[5] Slotine, Jean-Jacques.E, Li, Weiping. “Fundamentals of Lyapunov Theory”. *Applied Nonlinear Control*. (Prentice-Hall. New Jersey. 1991): 40–97.

[6] Baillieul, John, Samad, Tariq, Khalil, Hassan K. “Lyapunov’s Stability Theory”. *Encyclopedia of Systems and Control*. (Springer-Verlag. London. 2015): 685–689.

[7] Theodorou, Theodoros. “Concept, Effects of sail parameters, Control”. *Three-Axis Attitude Control of Solar Sails Utilising Reflectivity Control Devices*. (Surrey Space Centre. Guildford. 2016): 30–76.

[8] Bo Fu, Evan Sperber, Fidelis Eke. “Solar sail technology – A state of the art review”. *Progress in Aerospace Sciences*. **86**, 1–19. (2016)

[9] Wie, Bong. “Solar Sail Attitude Control and Dynamics, Part 1”. *Journal of Guidance, Control and Dynamics*. **27**(4), 526–535. (2004)

[10] Lappas, V., Adeli, N., Visagie, L., Fernandez, J., Theodorou, T., Steyn, W., Perren, M. “CubeSail: A low cost CubeSat based solar sail demonstration mission”. *Advances in Space Research*. **48**(11), 1890–1901. (2011)

[11] Borggräfe, Andreas, Heiligers, Jeannette, Ceriotti, Matteo, McInnes, Colin R. “Attitude control of large Gossamer spacecraft using surface reflectivity modulation”. *65th International Astronautical Congress*. (2014)

[12] Funase, Ryu, Shirawasa, Yoji, Mimasu, Yuya, Mori, Osamu, Tsuda, Yuichi, Saiki, Takanao, Kawaguchi, Jun’ichiro “On-orbit verification of fuel-free attitude control system for spinning solar sail utilizing solar radiation pressure”. *Advances in Space Research*. **48**(11), 1740–1746. (2011)

[13] Choi, Mirue, Damaren, Christopher J. “Structural Dynamics and Attitude Control of a Solar Sail Using Tip Vanes”. *Journal of Spacecraft and Rockets*. **52**(6), 1665–1679. (2015)

[14] Wie, Bong, Barba, Peter M. “Quaternion feedback for spacecraft large angle maneuvers”. *Journal of Guidance, Control, and Dynamics*. **8**(3), 360–365. (1985)

[15] D. Choukroun, I., Y. Bar-Itzhack, Y. Oshman. “Optimal-REQUEST Algorithm for Attitude Determination”. *Journal of Guidance, Control, and Dynamics*. **27**(3), 418–425. (2004)

[16] Demiryont, Hulya, Shannon, Kenneth C. “Variable Emittance Electrochromic Devices for Satellite Thermal Control”. *AIP Conference Proceedings*. **880**(1), 51–58. (2007)

[17] Rios-Reyes, L., and D. J. Scheeres. “Generalized model for solar sails”. *Journal of Spacecraft and Rockets*. **42**(1), 182–185. (2005)

APPENDICES

APPENDIX A. MATLAB CODE FUNCTIONS

Solar sail attitude control simulatior

```
%%%%%%%%%%%%%%%%%%%%%%%%%%%%%%%%%%%%%%%%%%%%%%%%%%%%%%%%%%%%%%%%%%%%%%%%%%%%%%%%
% -------------------- SOLAR SAIL ATTITUDE SIMULATOR -------------------- %
%%%%%%%%%%%%%%%%%%%%%%%%%%%%%%%%%%%%%%%%%%%%%%%%%%%%%%%%%%%%%%%%%%%%%%%%%%%%%%%%
%                                                                         %
% Institution: Universitat Politècnica de Catalunya (BarcelonaTech)       %
% Project: Guidance, Navigation and control of a very small solar sail    %
% Project directors: Jordi Gutierrez Cabello                              %
%                                                                         %
% Authors:                                                                %
% ----------------------------------------------------------------------- %
% Carlos Díez García - Universitat Politècnica de Catalunya (EETAC)       %
%                                                                         %
% Contributors:                                                           %
% ----------------------------------------------------------------------- %
% Carles Pié Rubió - Universitat Politècnica de Catalunya (EETAC)         %
% Víctor Navarro Juárez - niversitat Politècnica de Catalunya (EETAC)     %
% ----------------------------------------------------------------------- %
%                                                                         %
% Version: v1.0                                                           %
% Date of last modification: 24/10/2017 (MM/DD/YYYY)                      %
%                                                                         %
%%%%%%%%%%%%%%%%%%%%%%%%%%%%%%%%%%%%%%%%%%%%%%%%%%%%%%%%%%%%%%%%%%%%%%%%%%%%%%%%
                        close all; clear all; clc;
```

Time properties

```
nSteps = 10000000;
dT = 1;
t = [1:nSteps];
```

Solar Sail initial state

```
% Initial relative attitude in Euler angles
yaw             = deg2rad(randi(90)); % yaw angle in rads
pitch           = deg2rad(randi(90)); % pitch angle in rads
roll            = deg2rad(randi(90)); % roll angle in rads

% Initial relative quaternion from Euler angles [qs; qx; qy; qz]
q_lvlh_body_0   = angle2quat(yaw, pitch, roll)';

% Initial relative angular velocity
wBody_inicial   = deg2rad(0)*[1;1;1];
```

```
% x[1:4] = quaternion from ECI to Body
% x[5:7] = angular speed in Body frame
x = [q_lvlh_body_0 zeros(4,nSteps-1); wBody_inicial zeros(3,nSteps-1)];
```

Solar sail properties

```
OpticalProperties_ConfigFile;   % Optical properties of solar sail and RCD
A_rcd       = 42.84 * 1e-4;             % RCD area from [cm^2] to [m^2]
A_sail      = 10 - A_rcd;               % Solar sail area in [m^2]
r_CoM       = [0; 0; 0;];               % Centre of Mass in m
D_rcd_CoM   = [ 1.5484,     1.48296, 0; % CoP - CoM offset for each RCD
                1.48296,   -1.5484,  0;
               -1.5484,    -1.48296, 0;
               -1.48296,    1.5484,  0; ]';
lx        = 10;                                 % Solar sail length in m
ly        = 10;                                 % Solar sail width in m
lz        = 7.5e-6;                             % Solar sail height in m
mSail     = 540.77 * 1e-3;                      % Solar sail mass in kg
inertia   = [ (1/12)*(ly^2+lz^2)*mSail, 0, 0;
              0, (1/12)*(lx^2+lz^2)*mSail, 0;
              0, 0, (1/12)*(lx^2+ly^2)*mSail ];   % Inertia matrix in Kg·m^2
```

ADCS control

```
% Reference
q_c         = [1;0;0;0];    % reference quaternion from Body to LVLH
w_c         = [0;0;0];      % reference angular speed in Body frame
Sun_v       = [0;0;1];      % reference sun-line vector

% Actuator
Tmax_RCD = [5.5043e-08,5.5043e-08,0]; % Maximum torque delivered from RCD

% Constant Gains adjusted to match the maximum RCD torque
Kp = 7e-7;          % Proportional gain
Kd = 7e-5;          % Derivative gain
```

Initialize the plotting array to save time

```
qPlot       = zeros(4,nSteps); % Array of Quaternion from LVLH to Body
wPlot       = zeros(3,nSteps); % Array of relative angular rate in rad/s
Euler       = zeros(3,nSteps); % Array of relative Euler angles in °
RefTorque   = zeros(3,nSteps); % Array of reference torque from control law
RCDTorque   = zeros(3,nSteps); % Array of generated torque from RCDs
qError      = zeros(4,nSteps); % Array of Error Quaternion
SRPPlot     = zeros(3,nSteps); % Array of SRP torque in N/m^2
```

Run the simulation

```
for k = 1:nSteps
    % Retrieve Satellite state in t = k instant
    q_k       = x(1:4, k);
    w_k       = x(5:7, k);

    % Compute relative euler angles
    [relyaw, relpitch, relroll] = quat2angle(q_k');
    EulerAngles = [rad2deg(relyaw), rad2deg(relpitch), rad2deg(relroll)];

    % Compute alpha (angle between Sail's normal and Sun-line vector
    normal_v = quatrotate(q_k', Sun_v');
    alpha = 90-atan2d(dot(Sun_v, normal_v), norm(cross(Sun_v, normal_v)));

    % Apply PD control law for reference torque
    [T_reference, q_e]    = PDcontroller(q_k, q_c, w_k, w_c, Kp, Kd);

    % Compute SRP for RCD on/off and Sail surface
    F_sail      = SRP(alpha, A_sail, sail);
    F_rcdON     = SRP(alpha, A_rcd, rcdON);
    F_rcdOFF    = SRP(alpha, A_rcd, rcdOFF);

    % Compute Torque for RCD on/off
    T_rcdON     = F_rcdON   * D_rcd_CoM;
    T_rcdOFF    = F_rcdOFF  * D_rcd_CoM;

    % Apply RCD control law
    tRCD        = RCDcontroller(T_rcdON, T_rcdOFF, T_reference);
    tTotal      = tRCD;

    % Save interesting values of control mechanims
    wPlot(:,k)          = w_k;
    qPlot(:,k)          = q_k;
    Euler(:,k)          = EulerAngles;
    qError(:,k)         = q_e;
    RefTorque(:,k)      = T_reference;
    RCDTorque(:,k)      = tRCD;

    % Compute Following State
    x(5:7, k+1) = w_k + inertia\(tTotal - Cross(w_k,inertia*w_k)) * dT;
    x(1:4, k+1) = q_k + QIToBDot( q_k, w_k ) * dT;
end
```

Plotting

```
NominalPlots(t, Euler, qPlot, wPlot, RefTorque, RCDTorque);
```

Optical properties configuration file

```
% Solar sail surface
sail.epsilon_b   = 0.17; % Emittance back surface
sail.rho_d       = 0;    % Specular reflection only
sail.B_f         = 2/3;  % Lambertian front surface
sail.B_b         = 2/3;  % Lambertian back surface

sail.a          = 0.08;  % Absorbance
sail.epsilon_f  = 0.02;  % Emittance front surface
sail.rho_s      = 0.92;  % Specular reflectance

% RCD bleached state 'on'
rcdON.epsilon_b   = 0.17;
rcdON.rho_d       = 0;
rcdON.B_f         = 2/3;
rcdON.B_b         = 2/3;

rcdON.a          = 0;
rcdON.epsilon_f  = 0;
rcdON.rho_s      = 1;

% RCD coloured state 'off'
rcdOFF.epsilon_b   = 0.17;
rcdOFF.rho_d       = 0;
rcdOFF.B_f         = 2/3;
rcdOFF.B_b         = 2/3;

rcdOFF.a          = 0;
rcdOFF.epsilon_f  = 0;
rcdOFF.rho_s      = 0;
```

SRP function

```
function [F_tot] = SRP(alpha, A, d)
    %%%%%%%%%%%%%%%%%%%%%%%%%%%%%% SRP %%%%%%%%%%%%%%%%%%%%%%%%%%%%%%%%
    Re  = 149.5978707e9; % Distance between Earth and Sun (1AU) in [m]
    Ls  = 3.828e26; % Solar luminosity in [W]=[N·m/s]
    c   = 3e8; % Speed of light in [m/s]
    r   = 1.5e8 + Re + 1.5e9;   % Distance w.r.t the sun in [m]
                                %(L2 orbit radius + Sun-Earth distance
                                % + L2-Earth distance)

    We  = Ls/(4*pi*Re^2); % Solar energy flux measured at the Earth
                          % in [W/m^2]=[N/m·s]
    W   = We * (Re/r)^2;  % Solar energy flux in [N/m·s]
    P   = W/c; % SRP in [N/m^2]

    %%%%%%%%%%%%%%%%%% SRP force - Optical model %%%%%%%%%%%%%%%%%%%%%%
    F_nor = P*A*(cos(alpha)^2 + d.a*cos(alpha)*((d.epsilon_f * d.B_f ...
    - d.epsilon_b * d.B_b)/(d.epsilon_f + d.epsilon_b)) + ...
    d.rho_s*(cos(alpha)^2) + d.rho_d*d.B_f*cos(alpha));
    F_tan = P*A*(cos(alpha)*sin(alpha)*(1 - d.rho_s));
    F_tot = sqrt(F_nor^2 + F_tan^2);
end
```

PD control law function

```
function [L, q_e] = PDcontroller (q_t, q_c, w_t, w_c, kp, kd)
    q_e = [0;0;0;0];    % [qs; qx; qy; qz]

    q_conj  = [q_t(1);-q_t(2:4)];
    q_inv   = q_conj/norm(q_t)^2;

    % Error signal
    q_e = QMult(q_c,q_inv);
    w_e = w_t - w_c;

    % Control law
    L_p = - kp * q_e(2:4);
    L_d = - kd * w_e;

    L = sign(q_e(1)) * L_p + L_d;
end
```

RCD control law function

```
function tTotal = RCDcontroller(T_on, T_off, T_reference)
    tTotal = 0;
    diference=norm(T_reference);

    % Torque generated in each combination of reflectivity
    T_comb = [ T_on(:,1)             + sum(T_off(:,2:4),2),...
               T_on(:,2)             + T_off(:,1) + sum(T_off(:,3:4),2),...
               T_on(:,3)             + sum(T_off(:,1:2),2) + T_off(:,4),...
               T_on(:,4)             + sum(T_off(:,1:3),2),...
               sum(T_on(:,1:2),2)    + sum(T_off(:,3:4),2),...
               sum(T_on(:,2:3),2)    + T_off(:,1) + T_off(:,4),...
               sum(T_on(:,3:4),2)    + sum(T_off(:,1:2),2),...
               T_on(:,1) + T_on(:,4) + sum(T_off(:,2:3),2) ];

    for i=1:8
    valor = norm(abs(T_comb(:,i) - T_reference));
        if(valor<diference)
            diference = valor;
        tTotal = T_comb(:,i);
         end
    end
end
```

APPENDIX B. TECHNICAL SENSORS DATA-SHEETS

Ultralow Noise, Dual-Axis MEMS Gyroscope

Data Sheet **ADXRS290**

FEATURES

- MEMS pitch and roll rate gyroscope
- Ultralow noise: 0.004°/s/√Hz
- High vibration rejection over a wide frequency range
- Power saving standby mode
  - 80 µA current consumption in standby mode
  - Fast startup time from standby mode: <100 ms
- Low delay of <0.5 ms for a 30 Hz input at the widest bandwidth setting
- Serial peripheral interface (SPI) digital output
- Programmable high-pass and low-pass filters
- 2000 *g* powered acceleration survivability
- 2.7 V to 5.0 V operation
- −25°C to +85°C operation
- 4.5 mm × 5.8 mm × 1.2 mm cavity laminate package

APPLICATIONS

- Optical image stabilization
- Platform stabilization
- Wearable products

GENERAL DESCRIPTION

The ADXRS290 is a high performance MEMS pitch and roll (dual-axis in-plane) angular rate sensor (gyroscope) designed for use in stabilization applications.

The ADXRS290 provides an output full-scale range of ±100°/s with a sensitivity of 200 LSB/°/s. Its resonating disk sensor structure enables angular rate measurement about the axes normal to the sides of the package around an in-plane axis. Angular rate data is formatted as 16-bit twos complement and is accessible through a SPI digital interface. The ADXRS290 exhibits a low noise floor of 0.004°/s/√Hz and features programmable high-pass and low-pass filters.

The ADXRS290 is available in a 4.5 mm × 5.8 mm × 1.2 mm, 18-terminal cavity laminate package.

FUNCTIONAL BLOCK DIAGRAM

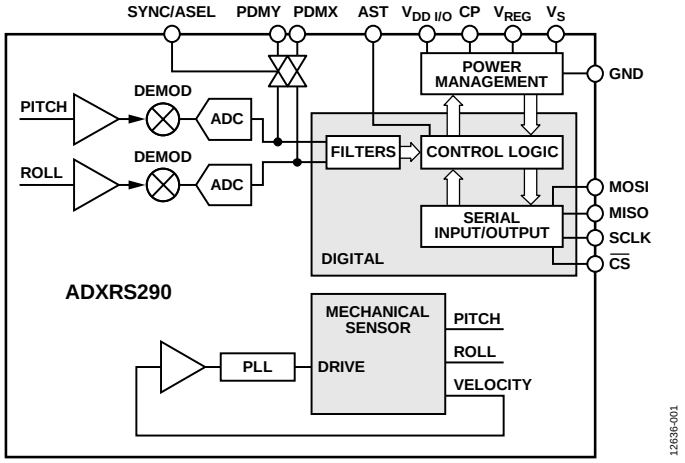

Figure 1.

Rev. A

Document Feedback

One Technology Way, P.O. Box 9106, Norwood, MA 02062-9106, U.S.A.
Tel: 781.329.4700

Technical Support www.analog.com

SPECIFICATIONS

Specified conditions at T_A = 25°C. V_S = $V_{DD\ I/O}$ = 3 V, angular rate = 0°/sec, bandwidth = dc to 480 Hz, C_S = C_{REG} = $C_{I/O}$ = C_{CP} = 1 µF, digital mode, temperature sensor = off, unless otherwise noted. All minimum and maximum specifications are guaranteed. Typical specifications are not tested or guaranteed.

Table 1.

Parameter	Test Conditions/Comments	Min	Typ	Max	Unit
MEASUREMENT RANGE	Each axis				
Output Full-Scale Range			±100		°/s
Resolution			16		Bits
Gyroscope Data Update Rate			4250		Hz
LINEARITY					
Nonlinearity			±0.5		% FS
Cross Axis Sensitivity			±2.0		%
SENSITIVITY					
Sensitivity			200		LSB/°/s
Initial Sensitivity Tolerance[1]	T_A = 25°C	−12	±3	+12	%
Change Due to Temperature	T_A = −20°C to +60°C		±1		%
OFFSET					
Offset Error	T_A = −20°C to +60°C		±9		°/s
NOISE PERFORMANCE					
Rate Noise Density	T_A = 25°C at 10 Hz		0.004		°/s/√Hz
FREQUENCY RESPONSE	Programmable (see the Setting Bandwidth section)				
−3 dB Frequency[2]					
Low-Pass Filter		20		480	Hz
High-Pass Filter	DC output setting available	0.011		11.3	Hz
Delay	30 Hz input, low-pass filter (LPF) = 480 Hz		<0.5		ms
POWER SUPPLY					
Operating Voltage Range (V_S, $V_{DD\ I/O}$)		2.7		5.0	V
Supply Current	Measurement mode		7.8		mA
	Standby mode		80		µA
Start-Up Time (Standby)	Power off to standby mode		<5		ms
Start-Up Time (Measurement Mode)	Standby to measurement mode (to within ±1°/s of final value)		<100		ms
TEMPERATURE SENSOR					
Resolution			12		Bits
Sensitivity			0.1		°C/LSB
OPERATING TEMPERATURE RANGE					
Operating Temperature Range		−25		+85	°C

[1] Initial sensitivity tolerance minimum and maximum specifications are guaranteed by characterization and are not tested in production.
[2] Guaranteed by design and are not tested in production.

High Performance, Digital Output Gyroscope

Data Sheet

ADXRS453

FEATURES

Complete rate gyroscope on a single chip
±300°/sec angular rate sensing
Ultrahigh vibration rejection: 0.01°/sec/*g*
Excellent 16°/hour null bias stability
Internal temperature compensation
2000 *g* powered shock survivability
SPI digital output with 16-bit data-word
Low noise and low power
3.3 V to 5 V operation
−40°C to +105°C operation
Ultrasmall, light, and RoHS compliant
Two package options
- **Low cost SOIC_CAV package for yaw rate (z-axis) response**
- **Innovative ceramic vertical mount package (LCC_V) for pitch and roll response**

APPLICATIONS

Rotation sensing in high vibration environments
Rotation sensing for industrial and instrumentation applications
High performance platform stabilization

GENERAL DESCRIPTION

The ADXRS453 is an angular rate sensor (gyroscope) intended for industrial, instrumentation, and stabilization applications in high vibration environments. An advanced, differential, quad sensor design rejects the influence of linear acceleration, enabling the ADXRS453 to offer high accuracy rate sensing in harsh environments where shock and vibration are present.

The ADXRS453 uses an internal, continuous self-test architecture. The integrity of the electromechanical system is checked by applying a high frequency electrostatic force to the sense structure to generate a rate signal that can be differentiated from the baseband rate data and internally analyzed.

The ADXRS453 is capable of sensing an angular rate of up to ±300°/sec. Angular rate data is presented as a 16-bit word that is part of a 32-bit SPI message.

The ADXRS453 is available in a 16-lead plastic cavity SOIC (SOIC_CAV) and an SMT-compatible vertical mount package (LCC_V), and is capable of operating across a wide voltage range (3.3 V to 5 V).

FUNCTIONAL BLOCK DIAGRAM

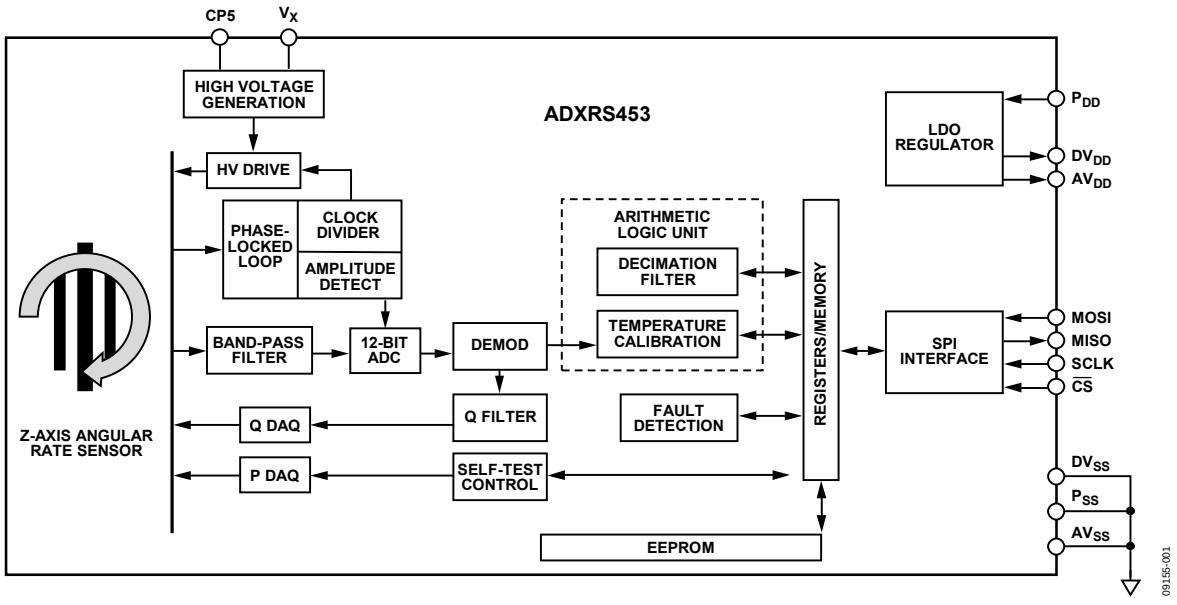

Figure 1.

Rev. B

One Technology Way, P.O. Box 9106, Norwood, MA 02062-9106, U.S.A.
Tel: 781.329.4700 www.analog.com
Fax: 781.461.3113

SPECIFICATIONS

$T_A = T_{MIN}$ to T_{MAX}, $P_{DD} = 5$ V, angular rate = 0°/sec, bandwidth = $f_0/200$ (~77.5 Hz), ±1 *g*, continuous self-test on.

Table 1.

Parameter	Test Conditions/Comments	Symbol	Min	Typ	Max	Unit
MEASUREMENT RANGE	Full-scale range	FSR	±300		±400	°/sec
SENSITIVITY	See Figure 2					
Nominal Sensitivity				80		LSB/°/sec
Sensitivity Tolerance	T_A = −40°C to +105°C		−3		+3	%
Nonlinearity[1]	Best fit straight line			0.05		% FSR rms
Cross-Axis Sensitivity[2]			−3		+3	%
NULL ACCURACY	T_A = 25°C			±0.4		°/sec
	T_A = −40°C to +105°C			±0.5		°/sec
NOISE PERFORMANCE						
Rate Noise Density	T_A = 25°C			0.015		°/sec/√Hz
	T_A = 105°C			0.023		°/sec/√Hz
LOW-PASS FILTER						
Cutoff (−3 dB) Frequency	$f_0/200$	f_{LP}		77.5		Hz
Group Delay[3]	f = 0 Hz	t_{LP}	3.25	4	4.75	ms
SENSOR RESONANT FREQUENCY		f_0	13	15.5	19	kHz
SHOCK AND VIBRATION IMMUNITY						
Sensitivity to Linear Acceleration	DC to 5 kHz			0.01		°/sec/*g*
Vibration Rectification				0.0002		°/sec/g^2
SELF-TEST	See the Continuous Self-Test section					
Magnitude				2559		LSB
Fault Register Threshold	Compared to LOCSTx register data		2239		2879	LSB
Sensor Data Status Threshold	Compared to LOCSTx register data		1279		3839	LSB
Frequency	$f_0/32$	f_{ST}		485		Hz
ST Low-Pass Filter						
Cutoff (−3 dB) Frequency	$f_0/8000$			1.95		Hz
Group Delay[3]			52	64	76	ms
SPI COMMUNICATIONS						
Clock Frequency					8.08	MHz
Voltage Input High	MOSI, $\overline{CS}$, SCLK		0.85 × P_{DD}		P_{DD} + 0.3	V
Voltage Input Low	MOSI, $\overline{CS}$, SCLK		−0.3		P_{DD} × 0.15	V
Voltage Output Low	MISO, current = 3 mA				0.5	V
Voltage Output High	MISO, current = −2 mA		P_{DD} − 0.5			V
Pull-Up Current	$\overline{CS}$, P_{DD} = 3.3 V, $\overline{CS}$ = P_{DD} × 0.15			60	200	µA
	$\overline{CS}$, P_{DD} = 5 V, $\overline{CS}$ = P_{DD} × 0.15			80	300	µA
MEMORY REGISTERS	See the Memory Register Definitions section					
Temperature Register						
Value at 45°C				0		LSB
Scale Factor				5		LSB/°C
Quadrature, Self-Test, and Rate Registers						
Scale Factor				80		LSB/°/sec
POWER SUPPLY						
Supply Voltage		P_{DD}	3.15		5.25	V
Quiescent Supply Current		I_{DD}		6.0	8.0	mA
Turn-On Time	Power-on to 0.5°/sec of final value			100		ms

[1] Maximum limit is guaranteed by Analog Devices, Inc., characterization.
[2] Cross-axis sensitivity specification does not include effects due to device mounting on a printed circuit board (PCB).
[3] Minimum and maximum limits are guaranteed by design.

nanoSSOC-A60

Sun Sensor for Nano-Satellites
Analog interface

Technical Specification, Interfaces & Operation

Specifications

Two orthogonal axes sun sensor
Wide field of view (FOV): ±60º
High accuracy in FOV: < 0.5º
Precision: < 0.1º
Power supply: 3.3V (5V under request)
Reduced size: 27.4 × 14 × 5.9 mm
Low weight: 3,7 g
Temperature range: -30 to +85 ºC

Qualification

> 100 kRad Total Ionizing Dose
Space-grade components
Space qualified internal 4Q sensor

Applications

Low cost satellite attitude determination
Accurate Sun position determination
Satellite solar panel positioning
Attitude Failure Alarm
Satellite positioning in specific trajectory points
Balloons and UAVs control

Nano Sun Sensor on a Chip (nanoSSOC) is a two-axis low cost sun sensor for high accurate sun-tracking and attitude determination. This device measures the incident light and provides 4 analog outputs which can be processed to obtain both azimuth and elevation angles.

nanoSSOC sun sensor is based on MEMS fabrication processes to achieve high integrated sensing structures.

Every sensor is individually characterized and calibrated. The use of materials as aluminum 6082 minimizes the ageing of the device under high energy particle radiation.

nanoSSOC-A60 has minimum size, weight and power consumption to be the perfect ADCS solution for nano-satellite platforms like Cubesats.

3. TECHNICAL SPECIFICATIONS

Parameter	Value	Comments
Angles reading		
Sensor type	2 axes	Orthogonal.
Field of view (FOV)	± 60 º	Angular size of the view cone
Accuracy	< 0.5 º	3σ error
Precision	< 0.1 º	
Electrical		
Supply voltage	3.3 V	5V under request
Average consumption	< 0.1 mA	Dark
Average consumption	< 2 mA	Light: 1360 W/m^2, AM0
Thermal		
Temperature range	- 30 to +85 ºC	
Mechanical		
Dimensions (L × W × H)	27.4 × 14 × 5.9 mm	
Weight	3,7 g	
Mount holes	M2.5 x2	
Connector	DF13A-10DP-1.25V(55)	From Hirose
Housing	Aluminum 6082	Alodine 1200S (ECSS-Q-70-71) Black anodized (ECSS-Q-ST-70-03C)
Qualification		
Total ionizing dose	> 100 kRad	Gamma radiation
Beam energy	6 MeV	Proton beam
Random vibration	14,1g @ 20-2000 Hz	
Shock	3000 g @ 1-100 ms	

Table 1. General specifications

IIS2DH

Ultra-low-power high-performance 3-axis accelerometer with digital output for industrial applications

Datasheet - production data

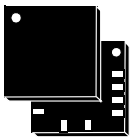

LGA-12 (2.0x2.0x1 mm)

Features

- Wide supply voltage, 1.71 V to 3.6 V
- Independent IOs supply (1.8 V) and supply voltage compatible
- Ultra-low power consumption down to 2 µA
- ±2*g*/±4*g*/±8*g*/±16*g* selectable full scales
- I^2C/SPI digital output interface
- 3 operating modes: low-power, normal, high-resolution mode
- 2 independent programmable interrupt generators for free-fall and motion detection
- 6D/4D orientation detection
- Motion detection & free-fall detection
- “Sleep-to-wake” and “return-to-sleep” functions
- Embedded FIFO
- Embedded self-test
- Embedded temperature sensor
- ECOPACK®, RoHS and “Green” compliant

Applications

- Robotics
- Anti-tampering devices
- Vibration monitoring
- Tilt/inclination measurements
- Impact recognition and logging
- Industrial tools and factory equipment
- Motion-activated functions

Description

The IIS2DH is an ultra-low-power high-performance three-axis linear accelerometer with digital I^2C/SPI serial interface standard output.

The IIS2DH has user-selectable full scales of ±2*g*/±4*g*/±8*g*/±16*g* and is capable of measuring accelerations with output data rates from 1 Hz to 5.3 kHz.

The device may be configured to generate interrupt signals by two independent inertial wake-up/free-fall events as well as by the position of the device itself.

The self-test capability allows the user to check the functionality of the sensor in the final application.

The IIS2DH is available in a small thin plastic land grid array package (LGA) and is guaranteed to operate over an extended temperature range from -40 °C to +85 °C.

Table 1. Device summary

Order code	Temperature range [°C]	Package	Packaging
IIS2DHTR	-40 to +85	LGA-12	Tape and reel

2 Mechanical and electrical specifications

2.1 Mechanical characteristics

@ Vdd = 2.5 V, T = 25 °C unless otherwise noted[a]

Table 3. Mechanical characteristics

Symbol	Parameter	Test conditions	Min.[1]	Typ.[2]	Max.[1]	Unit
FS	Measurement range[3]	FS bits set to 00		±2.0		*g*
		FS bits set to 01		±4.0		
		FS bits set to 10		±8.0		
		FS bits set to 11		±16.0		
So	Sensitivity	FS bits set to 00; Normal mode	3.52	3.91	4.30	mg/digit
		FS bits set to 00; High-resolution mode	0.88	0.98	1.07	
		FS bits set to 00; Low-power mode	14.06	15.63	17.19	
		FS bits set to 01; Normal mode	7.03	7.81	8.59	mg/digit
		FS bits set to 01; High-resolution mode	1.76	1.95	2.15	
		FS bits set to 01; Low-power mode	28.13	31.25	34.38	
		FS bits set to 10; Normal mode	14.06	15.63	17.19	mg/digit
		FS bits set to 10; High-resolution mode	3.52	3.91	4.30	
		FS bits set to 10; Low-power mode	56.25	62.50	68.75	
		FS bits set to 11; Normal mode	42.25	46.95	51.64	mg/digit
		FS bits set to 11; High-resolution mode	10.55	11.72	12.90	
		FS bits set to 11; Low-power mode	169.81	188.68	207.55	
TCSo	Sensitivity change vs. temperature	FS bits set to 00		±0.01		%/°C
TyOff	Typical zero-*g* level offset accuracy[4]	FS bits set to 00	-90	±40	+90	mg

a. The product is factory calibrated at 2.5 V. The operational power supply range is from 1.71 V to 3.6 V.

2.3 Electrical characteristics

@ Vdd = 2.5 V, T = 25 °C unless otherwise noted[c]

Table 5. Electrical characteristics

Symbol	Parameter	Test conditions	Min.	Typ.[1]	Max.	Unit
Vdd	Supply voltage		1.71	2.5	3.6	V
Vdd_IO	I/O pins supply voltage[2]		1.71		Vdd+0.1	V
Idd	Current consumption in normal mode	50 Hz ODR		11		µA
Idd	Current consumption in normal mode	1 Hz ODR		2		µA
IddLP	Current consumption in low-power mode	50 Hz ODR		6		µA
IddPdn	Current consumption in power-down mode			0.5		µA
VIH	Digital high-level input voltage		0.8*Vdd_IO			V
VIL	Digital low-level input voltage				0.2*Vdd_IO	V
VOH	High-level output voltage		0.9*Vdd_IO			V
VOL	Low-level output voltage				0.1*Vdd_IO	V
Top	Operating temperature range		-40		+85	°C

1. Typical specification are not guaranteed.
2. It is possible to remove Vdd, maintaining Vdd_IO without blocking the communication busses, in this condition the measurement chain is powered off.

c. The product is factory calibrated at 2.5 V. The operational power supply range is from 1.71 V to 3.6 V.